6 Young Stellar Objects and Protostellar Disks

Ana Inés Gómez de Castro
Fac. de CC Matematicas, Universidad Complutense de Madrid, Madrid, Spain

Abstract: Stars form out of molecular clouds with densities of $10^4 \, cm^{-3}$ and temperatures of 10 K. Clouds fragment into molecular cores covering a broad range of masses that give rise to the formation stellar associations, clusters and single stars. High mass star formation rapidly removes the environmental gas and dust having a large impact into cloud evolution. Low mass star formation is less aggressive with the environmental cloud. Young stellar objects (YSOs) display a wide range of properties depending on their mass, age and star forming environment. Very massive YSOs generate ultracompact HII regions embedded in the cores of molecular clouds. Their key observational properties are related with the action of strong and highly photoionizing radiation fields in the surrounding molecular cloud. They evolve in time scales of few Myrs into the main sequence. Low mass YSOs progress to the main sequence at a slower pace; the gravitational collapse is slowed down by the action of the molecular cloud magnetic field and their most conspicuous observational properties are related with dissipation of the magnetic energy carried out during star formation and enhanced by shear during the star building up.

Protostellar disks are a by-product of star formation. They are formed as angular momentum reservoirs during the gravitational accretion process that gives rise to the formation of new stars. They are observed around all types of YSOs however their properties and evolution depend on the nature of the parent star/stars. The opacity of the disk and its selfshielding properties against the stellar and the environmental radiation field determine the lifetime of protostellar disks that end as debris disks and planetary systems. Disks play a key role in the generation of the powerful bipolar outflows observed during star formation. Bipolar outflows are observed from the very early stages (10^4 years) of star formation and from all the mass spectrum of YSOs.

This chapter attempts to summarize our current understanding of single star formation and the joint evolution of the star-disk system towards the main sequence.
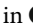
1 Introduction

Stars form out of dense gas in molecular clouds. Clouds fragment into molecular cores that afterward contract gravitationally to form either single or multiple stellar systems. Fragmentation requires rapid cooling, faster than the relevant dynamical timescales of the system, and depends on the physical properties and chemical composition of matter as described in detail in ❯ Chap. 4. Most of the stars are formed in multiple systems where the angular momentum of the original cloud is stored in a coupled spin-orbit system with a fraction of the angular momentum going into the orbits of fragments and another fraction into the collapsing fragments themselves. During star formation, the specific angular momentum decreases several orders of magnitude from $j \simeq 10^{23} \, cm^2 s^{-1}$ in molecular cloud material (scales of about 1 pc) to $j \simeq 10^{21} cm^2 s^{-1}$ in molecular cores (scales of about 0.1 pc) to reach finally $j \simeq 10^{17} cm^2 s^{-1}$ in the young stars entering the main sequence. During this process angular momentum conservation leads to the formation of angular momentum reservoirs, the protostellar disks, that grow as the stellar embryo does it and that have their own evolutionary scales.

The term Young Stellar Object (YSO) is introduced to define astronomical sources in this evolutionary phase from contracting objects within opaque dust cocoons to pre-main sequence (PMS) stars close to the zero age main sequence. Three major evolutionary phases can be defined in the formation of stars:

- *Phase I: Protostellar core evolution*: The evolution of gravitationally bounded molecular cores into protostellar cores. The evolution timescale is controlled by the turbulence field in the core.
- *Phase II: Main accretion phase*: The main accretion phase begins when turbulence support is overcome and non-homologous gravitational collapse produces a differentiation between the stellar embryo and the surrounding envelope. At the end of this phase, a central source that contains about half of the mass of the core is formed. Simultaneously a large protostellar disk is formed. During this evolutionary phase YSOs are denoted as class 0 YSOs (see Froebrich 2005 for a catalog). The stellar birthline is defined by the end of this phase.
- *Phase III: PMS stellar evolution and planetary disk formation*: Hydrostatic equilibrium evolution from the stellar birthline to the main sequence. At the same time, the protostellar disk evolves from a massive structure channeling the accretion flow into a passive planetary disk. During this process the disk luminosity varies several orders of magnitude. At the first stages, the stellar atmosphere is occulted by the heavy excess produced by the accretion flow and the remnant extinction of the envelope. As these decrease, the stellar atmosphere becomes recognizable. Finally, the young planetary disk is formed and the stellar evolution is decoupled from the disk evolution. Objects in these three phases are named as Class I, II, and III YSOs, respectively. These three classes trace mainly the evolutionary state of the disk (see Herbig and Bell 1988 for a catalog).

This chapter is aimed at describing the last two evolutionary steps: the properties and evolution of protostellar disks and their interaction with the growing star. This interaction is a rich source of physics being the most conspicuous in the creation of gravitational engines able to accelerate part of the accreting matter and eject it forming large bipolar outflows. The physics of pre-main sequence evolution is very complex and competing simple scenarios have been developed to tackle the different aspects of the problem. For this reason, this chapter has been divided into three sections dealing with the evolution of the three main components of YSOs: star, disk, and outflow. This division mimics the physical systems involved and the main areas of theoretical work; however, it is worth to remark that these three components are strongly coupled through gravity, radiation and magnetic fields. In addition, the identification of the contribution from each component to the observed radiation is not always straightforward leading to uncertainties in the interpretation of the data within a given theoretical framework. The spectrum of the prototypes to low mass and intermediate mass PMS stars, T Tau and AB Aur, respectively, are displayed in ❯ *Fig. 6-1*; the physical components that dominate the radiative output at each wavelength are indicated. A sketch of the structure of the inner ~1 AU of low mass YSOs is outlined in ❯ *Fig. 6-2*.

2   PMS Evolution: The Star

YSO precursors are gravitationally bounded protostellar cores evolving in magnetized molecular clouds. Protostellar cores' lifetimes have been estimated to be $3 - 5 \times 10^5$ years (Kirk et al. 2005; Onishi et al. 2002) which are about a factor of 2–3 larger than their
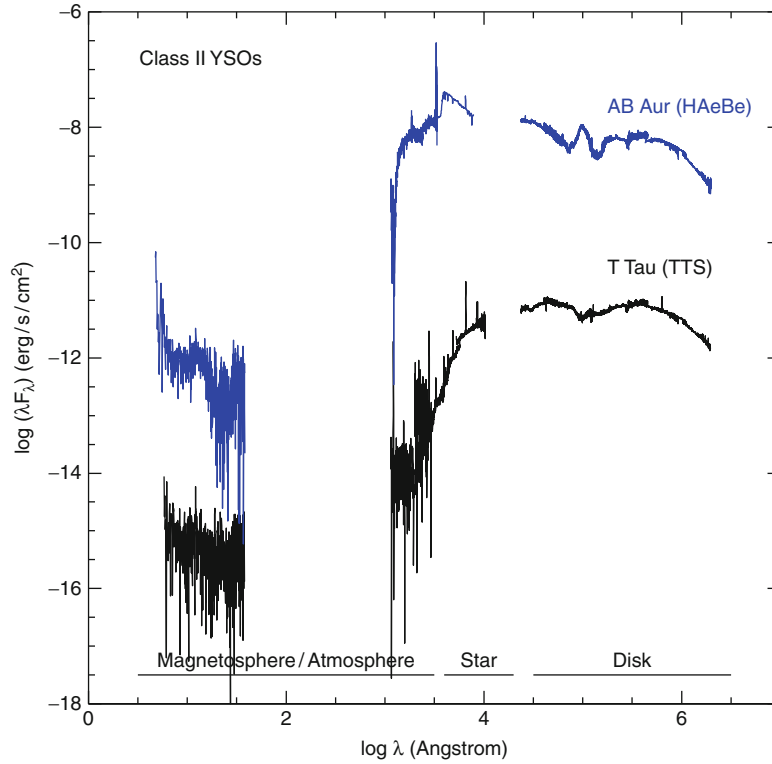
◨ Fig. 6-1
Spectral energy distribution of T Tau (*black*) and AB Aur (*blue*). The main contributors to the flux in each spectral range are marked at the bottom. T Tau flux is reduced by two orders of magnitude (−2 in the Y-axis scale) for the plot. AB Aur and T Tau are prototypes to class II YSOs of intermediate ($2M_\odot < M_* < 10M_\odot$) and low ($M_* < 2M_\odot$) mass, respectively

free-fall times[1] ($1.1 - 1.6 \times 10^5$ years) suggesting some degree of support during this phase. The support is most likely provided by turbulence. Molecular line emission from protostellar cores is very broad, typically $1-4\,\mathrm{km\,s^{-1}}$, thus highly suprathermal for the low temperatures of the cores.[2] As magnetic fields pervade the InterStellar Medium (ISM) HydroMagnetic (HM) turbulence is a natural source of support. In fact, the line broadening after subtraction of the thermal component scales with the cores' mean magnetic field (Myers and Goodman 1988). Molecular cores are weakly ionized[3] thus a strong coupling between ions and neutrals is required to

---

[1]The free-fall time for a spherical core of uniform density ρ_c is $t_{\mathrm{ff}} = (3\pi/32G\rho_c)^{1/2} = 1.08 \times 10^5\,\mathrm{year}\,(n_c/10^5\mathrm{cm^{-3}})^{-1/2}$, where n_c is the particle density of the core.

[2]Molecular cores' temperature is about 10 K and sound speed is $0.19\sqrt{T/10\,\mathrm{K}}\,\mathrm{km\,s^{-1}}$.

[3]The high density of molecular clouds shield the cores against the environmental UV radiation. The major source of ionization is cosmic rays that produce an ionization fraction of $\chi_e \simeq 4.5 \times 10^{-6} n_{\mathrm{H}}^{-1/2}(\mathrm{cm^{-3}})$ (McKee 1989).
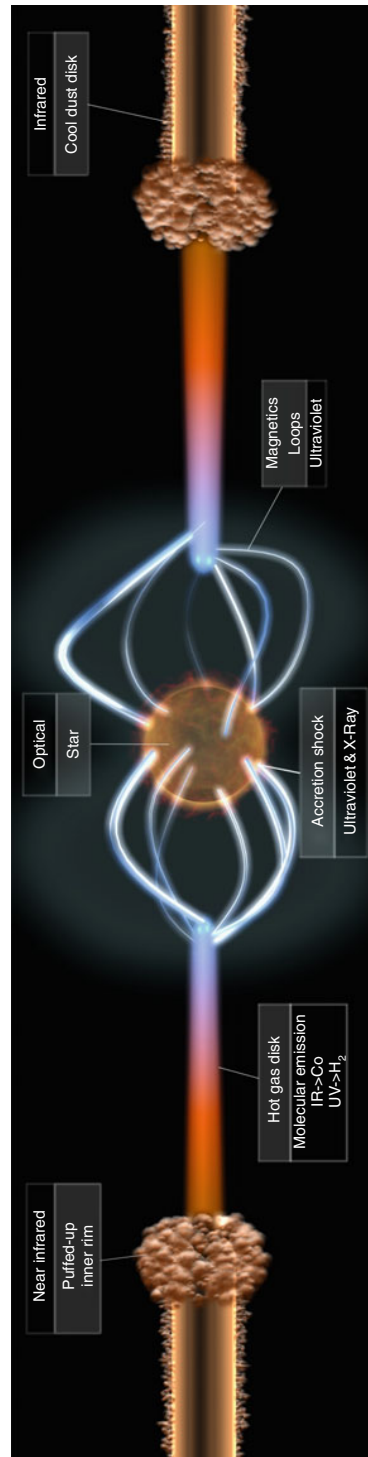
■ Fig. 6-2

Sketch of the inner structure of a low mass (<2$M_\odot$) YSO. The spectral ranges where the bulk of the energy of each component is radiated are indicated. *The inner border* **of the disk is the boundary with the stellar magnetosphere. Another important boundary is set by the dust melting point that separates the two thermal regimes of the disk: gas dominated versus dust dominated**

support cores against collapse by this mean. The ion-neutral collision frequency is

$$\nu_{n,i} \sim 10^{-9} s^{-1} \frac{<V>}{2 \text{ km s}^{-1}} n_i (\text{cm}^{-3}) = \gamma_{n,i} n_i (\text{cm}^{-3})$$

where n_i is the ions' particle density in the core and $<V>$ is the characteristic velocity of the gas motions and $\gamma_{n,i}$ the rate coefficient for ion-neutral collisions (Braginskii 1965). This frequency defines the ambipolar diffusion threshold. HM waves with frequencies higher than $\nu_{n,i}$ only operate on a small fraction of the mass of the core, the ionized component, and cannot support the core against collapse. HM waves with frequencies shorter than $\nu_{n,i}$ are able to support molecular cores against collapse. HM waves with frequencies $\sim\nu_{n,i}$ dissipate by the neutrals' drag force heating the cores by ambipolar diffusion. The ambipolar diffusion timescale or the timescale for momentum transfer between ions and neutrals in molecular clouds was derived by Arons and Max (1975) to be,

$$\tau_{AD} = 1.6 \times 10^5 \text{year} \mu_{n,i} \left(\frac{P}{10^5 \text{year}} \right)^2 \frac{x_i}{10^{-6}} \frac{\gamma_{n,i}}{10^{-9}} \frac{n(H_2)}{10^4 \text{ cm}^{-3}}$$

with $\mu_{n,i} = m_i/(m_i + m_n)$, $n(H_2)$ the density of the molecular gas, χ_i the ionization fraction (n_i/n_n), and P the characteristic timescale of the propagating mode. τ_{AD} depends on the ionization fraction of the cores and thus on the strength and penetration of high-energy (ultraviolet, X-ray) radiation. This timescale is comparable to the protostellar cores' lifetime determined from observations confirming that pseudo-hydrostatic contraction is a good approach to model the first evolutionary stages of star formation. For this reason, Bonnor–Ebert spheres are often taken as the departure point for dynamical calculations of the gravitational collapse from core to class 0 YSOs.

Hydrostatic contraction of self-gravitating spheres was first studied by Bonnor, Ebert, and McCrea in the late 1950s. Virial equilibrium in a self-gravitating molecular cloud leads to a modified equation of state of the form $pV = (M/\mu m_H)k_B T + (1/3)\epsilon_g$, where p, V, M, μm_H, and T are the cloud pressure, volume, mass, mean molecular weight, and temperature, respectively; ϵ_g is the potential energy of the self-gravitating cloud, and k_B the Boltzmann constant. The hydrostatic evolution of the gas leads to a modified Emden equation whose solution departs from the isothermal ideal gas law, that is, gravity prevents the volume to decrease smoothly as pressure rises; instead, there is a critical volume (radius) above which self-gravitation drives the object contraction. This critical radius is given by $r_c = 0.06 \text{ pc} \times (T/10 \text{ K})^{1/2} (n/10^4 \text{ cm}^{-3})^{-1/2}$ where T and n are the temperature and particle density of the self-gravitating cloud (see Bonnor 1957 for a discussion on the relation between this critical length and the Jeans length). A critical mass can also be defined, the so-called Bonnor–Ebert mass, given by $M_{B-E} = 1.21 M_\odot (T/10 \text{ K})^{3/2} (n/10^4 \text{ cm}^{-3})^{-1/2}$.

YSOs begin their life as the dynamical collapse begins. Gravitational infall is nonhomologous regardless of the choice of initial or boundary conditions; a stellar embryo rapidly develops in the center of the core; free fall depends inversely on the density and the collapse proceeds more rapidly in the center where the density is the highest. The density profile adopts the form outlined in ❯ *Fig. 6-3* with a central plateau of uniform density (the rapidly contracting inner part of the core) and an envelope with density distribution $\rho(r) \propto r^{-p}$ with $p \sim 2$ in the outer parts of the contracting core (Larson 1969). Density gradients measured in isolated low mass protostellar cores follow closely this distribution though the slope is slightly shallower with $p \sim 1.5 - 2$ over the external $1.4 \times 10^3 - 10^4$ AU (Shirley et al. 2000, 2003). When the central density rises above some 10^{10} cm^{-3} the heat generated by the release of gravitational energy in the contraction is not any longer freely radiated away and compression becomes adiabatic
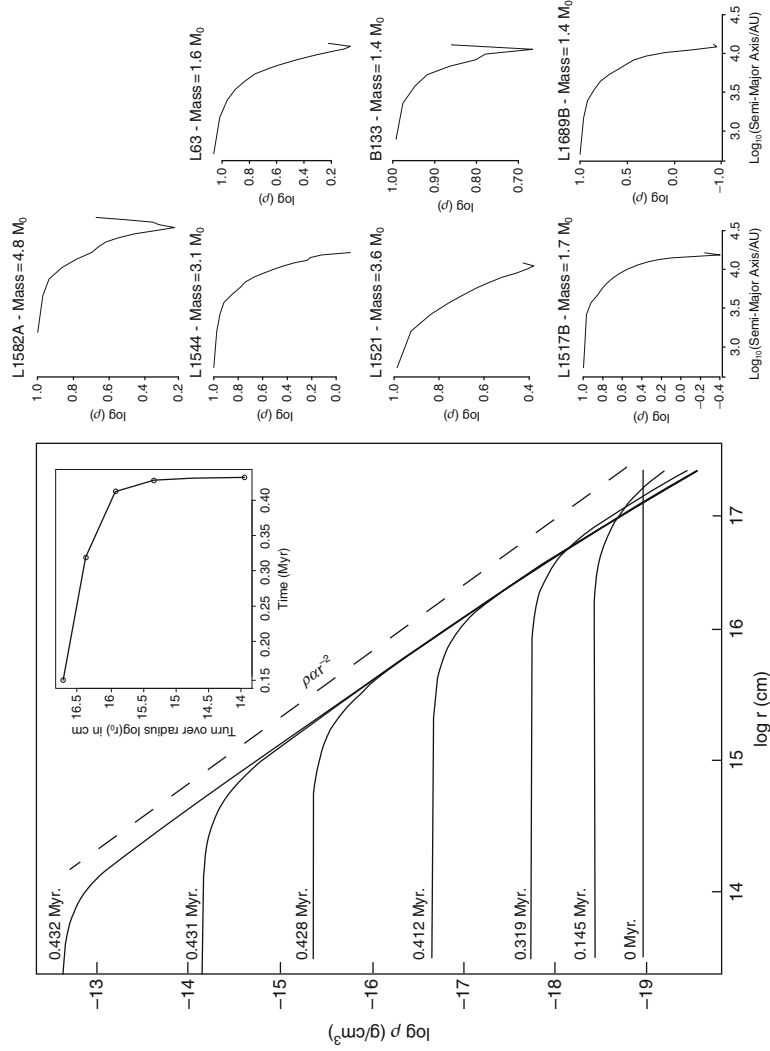
■ **Fig. 6-3**

The evolution of core-envelope differentiation during the gravitational collapse is displayed in the *left panel* for a self-gravitating solar mass protostellar core with initial uniform density (from Larson 1969). The molecular core central density rises. The envelope density decreases as "∼ 1/r^2." There is a turnover point in the density distribution that shifts to smaller radii as the collapse progresses as shown in the *upper inset*. The observed density radial distribution for the cores mapped by Kirk et al. (2005) is plotted in the *right panels*. The measured surface densities have been converted into volumetric densities assuming that the emitting cores are Bonnor–Ebert spheres with the radii derived by Kirk et al. (2005)

in the stellar embryo. The inner core contracts slowly hydrostatically alike while the remnant envelope keeps free-falling. Several readjustments of the protostellar core take place during this period caused mainly by the variations in the internal energy of the embryo associated with H_2 dissociation, dust processing, and the physics of the boundary layer and the shock front between the infalling external layers of the protostellar core and the growing embryo. The main accretion phase starts when the kinetic energy of the infalling material is negligible compared with its thermal energy and ends when approximately half of the total mass has fallen into the core. At this point the kinetic energy influx begins to decrease since the rise in the infall velocity $(V_{ff} = (2GM/R)^{1/2})$ cannot compensate the decrease in the density of the infalling material.

Observationally, objects during this period are named class 0 YSOs and are classified as such by either having a central compact centimeter radio source or by displaying extended and centrally peaked submillimeter continuum emission from the protostellar core. Additional criteria are a high ratio of submillimeter to bolometric luminosity ($L_{smm}/L_{bol} > 0.005$ with L_{smm} measured longward of $350\,\mu$m) which basically measures the mass ratio between the embryo and the rest of the core (Andre et al. 2000). Young embryos can also be detected by means of the powerful bipolar outflows they generate. A good catalog of class 0 YSOs has been compiled by Froebrich (2005).

Accretion causes a variation of the Kelvin–Hemholtz timescale, $\tau_{K-H} = GM_*^2/R_*L_* = 3.2 \times 10^7 \text{year} (M_*/M_\odot)^2 (R_*/R_\odot)^{-1} (L_*/L_\odot)^{-1}$, the timescale on which the star can radiate its thermal energy. τ_{K-H} increases as the star grows, and the growth rate is set by matter infall. After the main accretion phase, the temperature of the surface layers of the embryo decreases, as well as its luminosity, and the energy radiated from the surface of the embryo comes primarily from the interior instead of from the kinetic energy inflow. A convection zone develops and the star enters into the convective phase of the pre-main sequence (PMS) evolution (the so-called Hayashi track in low mass stars PMS evolution). At this point, the *stellar PMS evolution* begins. Hydrostatic equilibrium is appropriate to describe the main physics; accretion is often included as an external parameter that mildly affects the stellar structure.

Modeling of this evolution often begins assuming central temperatures low enough to guarantee that nuclear energy generation rates are negligible relative to gravitational energy generation rates but high enough to guarantee that hydrogen and helium are ionized throughout most of the star (Iben 1965). Central-outward integrations are matched with surface-inward integrations. PMS evolutionary tracks are computed from an uncertain initial mass–radius relationship. Key ingredients are the equation of state (Mihalas et al. 1988; Pols et al. 1995; Rogers et al. 1996; Saumon et al. 1995), the opacity tables (Alexander and Ferguson 1994; Iglesias and Rogers 1996), and the reaction rates (Caughlan and Fowler 1988). Most of the models assume gray atmospheres and adopt the standard Mixing Length Theory (MLT) treatment (Boehm-Vitense 1958) in which the free parameter, α_{MLT}, measures the ratio between the mixing length and the pressure scale height; this parameter is tuned in a range between 1 and 2. D'Antona and Mazzitelli (1997) have introduced a different formalism to describe turbulent convection in the models that takes into account the energy redistribution among different size eddies within the turbulence cascade, following the Kolmogorov prescription based on Canuto and Mazzitelli (1991) treatment. Direct attempts to include the effect of accretion have been led by Siess and Forestini (1996) and Behrend and Maeder (2001). Accretion implies a flow of fresh deuterium into the star; the rapid rate of the reaction $^2H(p,\gamma) \to \,^3He$ (barely few hundred years) and the fast penetration of deuterium are able to influence the global stellar evolution (Siess et al. 1997). PMS evolutionary tracks from non-accreting PMS stars (D'Antona and Mazzitelli 1997) and accreting PMS stars (Siess et al. 2000) are plotted in ❯ *Fig. 6-4*.
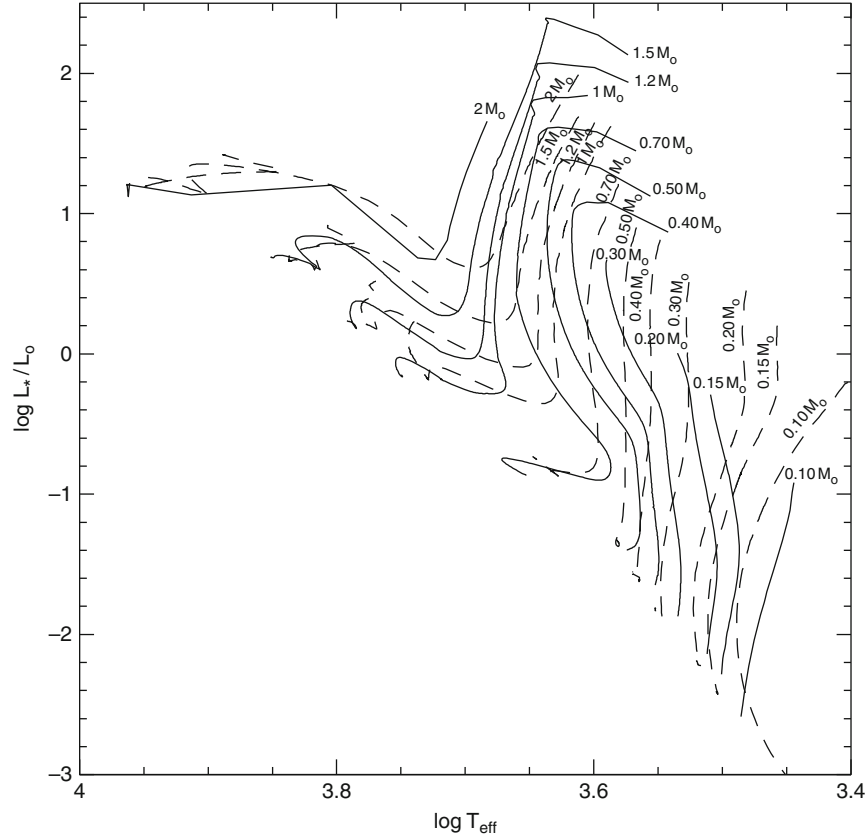
◼ **Fig. 6-4**
Pre-main sequence evolutionary tracks are shown for low mass stars. *Continuous lines* represent the tracks obtained by D'Antona and Mazzitelli (1997) based on a turbulence cascade approach to treat energy transfer in the convective layer. Siess et al. (2002) tracks are shown with *dashed lines*. They include the effect of fresh deuterium accretion during the PMS evolution

A fundamental calibration of the PMS evolutionary tracks is difficult. The amount of sources with known dynamical masses is small: four PMS eclipsing binaries – RS Cha (Andersen 1991), TY CrA (Casey et al. 1998), V1174 Ori (Stassun et al. 2004) and RXJ0529+0041 (Covino et al. 2004), and three spectroscopic binaries – AK Sco (Andersen et al. 1989), UZ Tau A (Simon et al. 2000) and RXJ0529+1210 (Mace et al. 2009). Keplerian disks orbiting around PMS stars also provide dynamical measurements of the stellar mass. Spatially resolved CO molecular emission has been detected from nine of them (MWC 480, LkCa 15, DL Tau, GM Aur, DM Tau, CY Tau, BP Tau, GG Tau A, and UZ Tau E) by Simon et al. (2000). The mass–luminosity relationship derived from these few observations is compared with that derived from the theoretical tracks in ❯ *Fig. 6-5*. There is not a clear mass–luminosity trend and the deviations between the dynamical masses and the ones derived from evolutionary tracks fitting are about a 10–50%. This comparison can be further extended including double PMS stars and early-main sequence
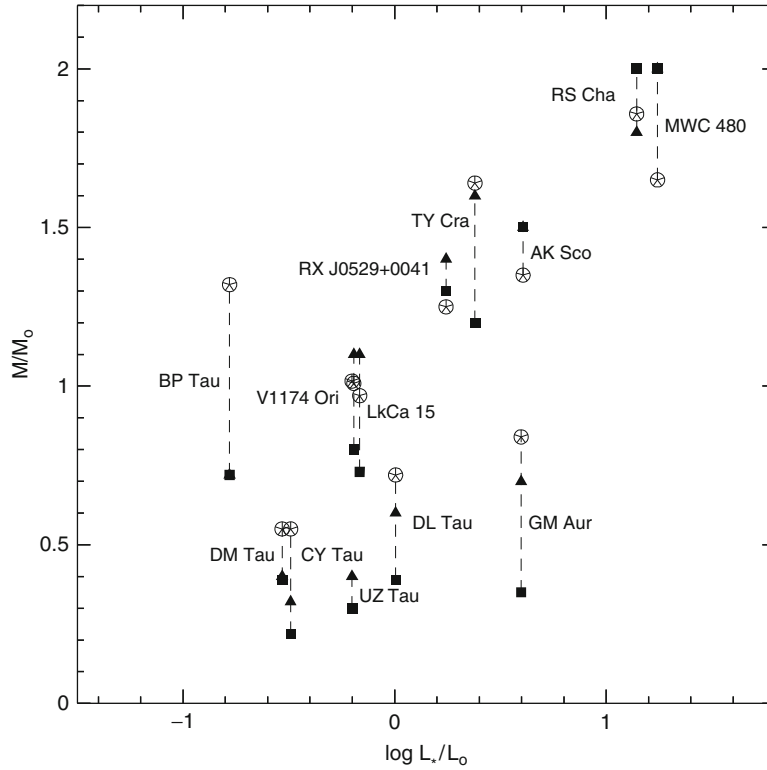
⬛ Fig. 6-5

Mass–luminosity diagram for the PMS stars with known dynamical masses. Dynamical masses are marked with circled *stars*, masses derived from PMS tracks are marked with *triangles* and *squares* for Siess et al. (2002) and D'Antona and Mazzitelli (1997) tracks, respectively

binaries for which dynamical masses are also available. As shown by Hillenbrand and White (2004), there is generally good agreement between predicted and dynamical masses both for PMS and early main sequence stars in the mass range 1.2–2 $M_\odot$. Below this threshold, models underestimate the stellar masses, being the trend more significant for the lower mass end, from early M-type stars to 0.1–0.2 $M_\odot$ stars. At this end of the mass spectrum, the role of accretion disks in PMS evolution extends longer in time.

3 PMS Evolution: The Disk

Disks form because free fall drives rotating cores to its minimum energy configuration, where most of the mass is concentrated in the center and most of the angular momentum is stored in a distant reservoir of negligible mass, as in the Solar System. They are observed around YSOs independently of their mass and evolutionary phase with the only possible exception of early O-type stars. As early as a free-fall time, a flattened structure forms around the growing stellar embryo. In this lapse, material with negligible angular momentum has already been accreted

onto the stellar embryo and the envelope material begins to feed massively the flattened reservoir in centrifugal equilibrium around the star. About this time, a "*mechanism*" sets in the disk that allows transporting the high angular momentum material from the disk into the star, coupling stellar growth to disk evolution. This mechanism acts efficiently on the gas component and, as disks loose gas, the accretion rate decreases. In about few Myrs, the gas to dust mass density ratio falls from 100, the fiducial ISM value, to less than 4 in transitional disks (see Collins et al. 2009) and later to values <<1 in debris disks as, for instance, β Pic disk (Roberge et al. 2006). In ❯ *Fig. 6-6* (from Looney et al. 2007), both components of the disk (gas and dust) are displayed for a class 0 YSO: L1157. The extinction of the environmental infrared radiation by the dust in the disk produces the dark lane. The molecular (CO) gas radio emission from the disk is also plotted as a contour map in the lower left inset. Perpendicular to them, there is a prominent bipolar outflow, mainly constituted of molecular gas with two clear components: the hot shocked gas, at temperatures ≥2,000 K, radiating in the infrared H_2 lines and the cold (<100 K) entrained gas radiating at radio frequencies in the CO line. As the radial extent of disks is some thousands of AU, they are less conspicuous than the outflows that may extend over more than a parsec. As other astrophysical disks, protostellar disks are associated with the
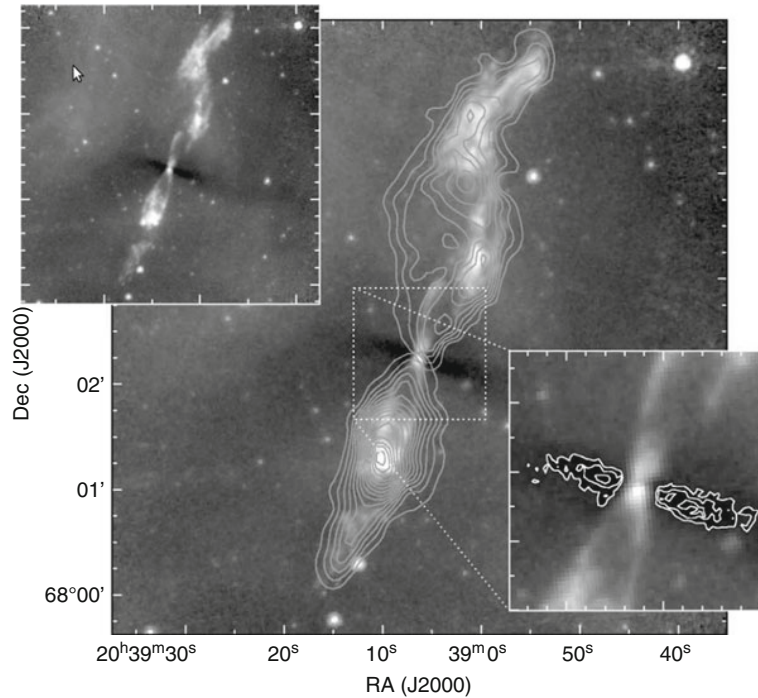
■ **Fig. 6-6**

Far infrared emission/absorption of the class 0 YSO: L1157 obtained with IRAC (Looney et al. 2007). Emission is produced along the outflow by molecular radiation. Absortion of the environmental infrared radiation from the dusty disk produces a dark lane perpendicular to the outflow, as shown in the upper inset. The molecular bipolar outflow is represented in the main panel. In the bottom right panel, the CO 2-1 emission from the molecular gas disk (from Bachiller et al. 2001) is overlaid on the dusty disk

formation of powerful bipolar outflows which are often the earliest observational signature of star formation. The connection between disks and outflows is described in ❯ Sect. 4.

There are two main differences between protostellar and other types of astrophysical disks such as the disks around active galactic nucleii or white dwarfs. Firstly, the thermal properties of the disk are controlled by the dust and depend strongly on the optical properties and thickness of their icy coatings as well as on the dust grains' size distribution. As a result, radiative processes are significantly more difficult to constraint than in the usual astrophysical disks made of simple atomic gas. Secondly, protostellar disks are not formed by smooth mass transfer between binary companions but as a result of gravitational collapse. Early stages, when the disk grows out of the envelope can be observed opening the way to the study of the physics of disk formation.

Disks are observed around YSOs at all evolutionary stages from the early class 0 stages to the late class III sources. *This sequence traces the history of accretion and disk evolution.* In this section, the current knowledge on the properties, structure, and evolution of protostellar disks is reviewed.

3.1 Morphology of Protostellar Disks

The nearest star forming regions are in a ring of radius 140 pc around the Sun. This ring marks the molecular walls of the Local Bubble in the ISM and forms part of a local kinematical and physical structure in the Galaxy known as the Gould's Belt (see Appendix A). Only very few and low mass class III YSOs are placed closer to the Sun, namely, TW Hya at 56 pc or the more evolved AB Dor at 15 pc. Thus, the distance of 140 pc sets the target angular resolution for disks' studies: 7 mas to resolve 1 AU scales or 0.07 mas to resolve the boundary between the star and the disk. Currently, the only way to achieve such a high resolution is by means of interferometry at optical and infrared wavelengths. Typical facilities have baselines of about 100 m and probe wavelengths of 1–13 μm providing spatial resolutions of 2–10 mas or 0.25–1.25 AU. These wavelengths trace hot dust emission (300–1,800 K) from the disk inner AU. The main structural properties of protostellar disks are described below.

3.1.1 The Inner Cavity Filled in with Hot Gas

The best studied targets are the Herbig Ae/Be stars (HAeBe stars). Herbig stars are YSOs in *Phase III* with masses of 2–10 solar masses that correspond to spectral types A to B. They are more luminous than the low mass (<2M$_\odot$) YSOs also known as T Tauri Stars or TTSs. Disks show as extended ellipses due to the projection of the circular disk on the plane of the sky. At 1–4 μm, disk emission is expected to be dominated by hot dust at the disk surface that scatters the stellar radiation. In fact, there is a strong correlation between the measured disk radii (r) and the luminosity of the central stars (L_*): $r \propto L_*^{1/2}$ (Millan-Gabet et al. 2007) as shown in ❯ *Fig. 6-7*. The observed disks radii are too large for the inefficient grazing incidence illumination of the disk surface. Direct illumination by the star is required instead, i.e., an inner disk cavity devoid of dust must exist around the star. Measured radii are consistent with the dust sublimation radii of relatively large dust grains (≥1μm) with sublimation temperatures in the range 1,000–1,500 K. The existence of this dust sublimation ring has been independently inferred from the bump in the near infrared energy distribution of Herbig stars (Natta et al.
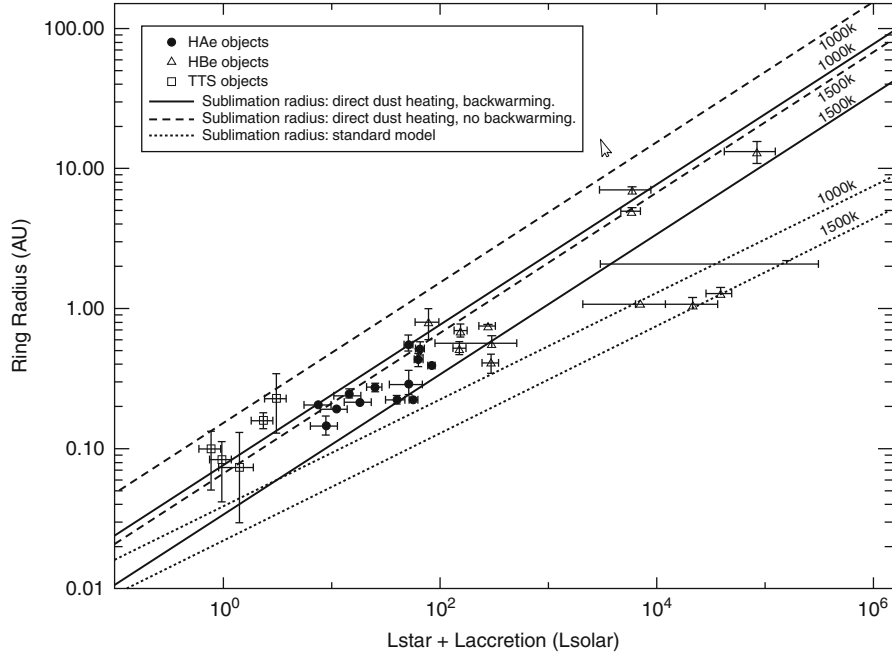
■ Fig. 6-7

Measured sizes of HAeBe and TTSs objects versus central luminosity and comparison with subli-mation radii for dust directly heated by the central luminosity (*solid and dashed lines*) and for the oblique heating of flaring disks (*dotted line*) after Millan-Gabet et al. (2007)

2001). The inner rim of the dusty disk is expected to be puffed-up by hydrostatic equilibrium but its vertical structure is still unclear.

The inner cavity of the disk is filled in with hot gas that is well traced by the CO funda-mental ($\Delta v = 1$) ro-vibrational transition at 2.3 μm. CO is an abundant molecule with high dissociation energy that can survive to temperatures of 4,000–5,000 K and is observed in nearly all CTTS (Najita et al. 2003). Many line profiles show the classic double-peaked profile pro-duced in rotating rings. The location of the emission region can be derived assuming Keplerian rotation in a thin disk. The profile also contains information on the radial variation of the gas emission. Radial variation of the gas temperature and column density can also be constrained if the first overtone band ($\Delta v = 2$) at 4.7 μm or other transitions from the same molecule are detected. The inner gas radius peaks about 0.04 AU and it is generally smaller than the corota-tion radius,[4] while the inner rim in the dust distribution is above this value. In addition, strong continuum emission has been detected in the far ultraviolet (1,300–1,700 Å) from some TTSs with bright molecular disks and inner disk gaps of few AU (Ingleby et al. 2009). This emission is likely due to energetic photoelectrons mixed into the molecular layer, providing additional evidence on the existence of a hot component in the inner disk.

---

[4]Corotation radius is the disk radius at which the Keplerian frequency equals the angular velocity of the star. Typical rotation velocities of YSOs range between 2 and 15 km s^{-1}; thus, the corotation radius is: $r_{\text{corot}} = 0.08$ AU$(M_*/M_\odot)^{1/3}(P/8\text{d})^{2/3}$, with P the rotation period of the star.
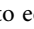
3.1.2 Disks Are Flared

The infrared spectrum of disks depends on the geometry of the disk and the composition of the dust. "Bowl-shaped" flared disks are much more efficient at capturing stellar photons than flat disks since (1) the geometrical covering factor of the stellar radiation field is higher and (2) the radiation incidence angle is closer to the normal to the disk surface.

Disk flaring is required to explain the spectral energy distribution (SED) of TTSs and HAeBe stars. In the 1–10 μm range, SEDs can be fitted by power laws ($\nu S_\nu \propto \nu^s$) with slopes, s, that range between 0.6 and 1 for the TTSs and between –1 and 1 for HAeBe stars. These slopes are softer than those expected from standard irradiated disks ($s = 4/3$) suggesting that the outer rings of the disk, the ones that radiate at the longest wavelengths, are capturing the stellar photons more efficiently than expected, i.e., disks are flared.

The upper, atmospheric disk layers can be mapped directly by means of the 8–13 μm radiation produced by the warm dust; infrared interferometers allow to probe scales of 1–4 AU. The radius of the region radiating at 8–13 μm is larger in HAeBe stars with strong flux in the far infrared[5] (Leinert et al. 2004) that are expected to have more flared disks. The measured radii are however, smaller than predicted by simple flared disk models (Millan-Gabet et al. 2001) suggesting an extra shadowing of the stellar radiation illuminating the puffed up inner rim of the dusty disk, as the despicted in ❯ *Fig. 6-2*.

In addition, radio interferometry at millimetric wavelengths allows to explore the gas distribution as traced by the CO emission at scales >50 AU. ^{12}CO($J = 2 - 1$) emission is produced at the disk surface and the radial distribution of CO kinetic temperature also agrees with the expectations of flared disks.
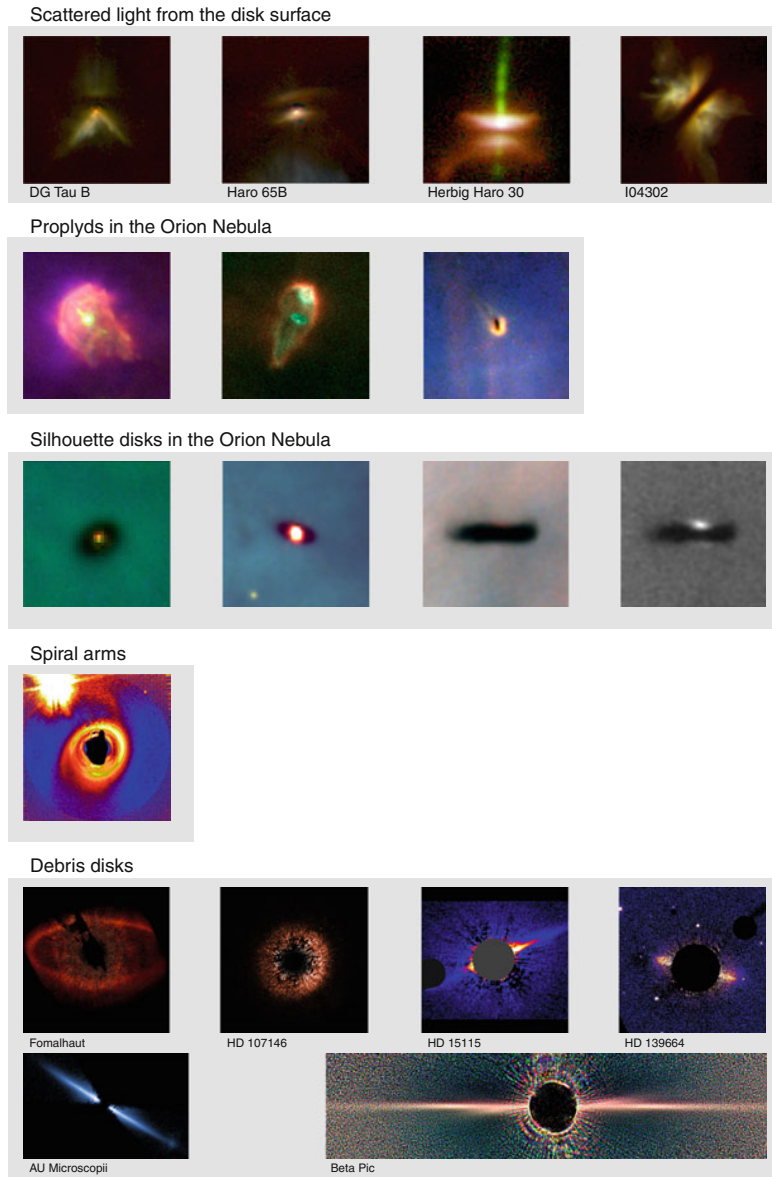
3.1.3 Dusty Atmospheres and Warps

At 0.4–1 μm scales, high resolution direct imaging is feasible with the Hubble Space Telescope (HST) and Adaptive Optics from the ground. The stellar radiation scattered by the circumstellar dust allows mapping the distribution and properties of the dust in the inner 500 AU with spatial resolution of about 100 mas (14 AU). Class I and II YSOs have thick dust disks that absorb the stellar radiation producing a dark lane in the images when disks are observed close to edge-on (see ❯ *Fig. 6-8*). This lane also acts like a natural coronograph that blocks direct stellar light providing high contrast for direct imaging. Further information is obtained from highly disturbed disks detected by their blockage of the environmental radiation, the so-called silhouette disks. Coronographs have also been used to block the stellar radiation and increase the dynamical range in the images; they typically block the inner, and more interesting, 0."5 (70 AU). However, despite all the efforts, most of the YSOs disks remain undetectable.

There are about 15 edge-on systems known with outer radii[6] ranging from 30 AU in IRAS 04325+2402 (Hartmann et al. 1999) to 620 AU in Orion 114–426 (Shuping et al. 2003). The vertical distribution of dust in the disks is derived from these images (see details in Watson et al. 2007). Disk scale heights are larger in systems with outflows like HH 30 where it reaches 6.3 AU at 50 AU from the star. Scattering dust grains are dominated by small particles that have

---

[5]HAeBe stars are classified into two groups according with s: Group I with $s = -1 - 0.2$ and strong far infrared excess and Group II with $s = 0.2 - 1$ and weak far infrared excess (Meeus et al. 2001).
[6]Disk may continue beyond the optical nebula

Scattered light from the disk surface

DG Tau B   Haro 65B   Herbig Haro 30   I04302

Proplyds in the Orion Nebula

Silhouette disks in the Orion Nebula

Spiral arms

Debris disks

Fomalhaut   HD 107146   HD 15115   HD 139664

AU Microscopii   Beta Pic

◼ **Fig. 6-8**

High resolution images of YSOs' disks obtained with the Hubble Space Telescope. From *top to bottom*: edge-on YSOs illuminating the dusty atmosphere of the disks in a quiet molecular cloud; proplyds or disrupted YSOs moving in the photoionized environment of the Orion star forming region; silhouette disks observed against the background radiation in Orion; AB Aur disk where hints of spiral structure has been detected; debris disks, with a low gas content illuminated by the star: rings, warps, and double structures are observed (Padgett et al. 1999; Bally et al. 2000; Clampin et al. 2003; Kalas et al. 2006, 2007, 2008; Krist et al. 2005; Golimowski et al. 2006)

much higher scattering cross section at shorter wavelengths. There is also evidence of grain size growth toward the disk midplane. Remnant circumstellar dusty envelopes have been detected in several systems. Occasionally, morphological variations are detected in the images. The most intriguing ones have been observed in HH 30; the reflection nebula varies on timescales ≤1 year that cannot be accounted by variations in the large-scale structure of the disk but rather on the illumination from the inner 1 AU. Whether this is yet another manifestation of the variable extinction events produced at the inner rim of the disk or in disk warps (as the detected in AA Tau by O'Sullivan et al. 2005) is still under debate.

3.2 Disk Mass

Molecular emission provides direct measurements of the gas content of the disk and its velocity pattern. The gas to dust mass ratio is not constant in YSOs' disks; close to the disk midplane most of the gas is frozen out into dust grains while dust grains are melted in the surface areas (Rettig et al. 2006). On average, the dust to gas mass ratio in protostellar disks is considered to be about a hundred, similar to that observed in the ISM. For this ratio, the column densities of YSOs disks can be approximated to be $\Sigma(r) = 0.8\,\mathrm{g\,cm}^{-2}(r/100\,\mathrm{AU})^{-1.5}$ from CO interferometric measurements (Dutrey et al. 2007).

Disk rotation has been investigated in a limited amount of YSOs' disks since CO interferometry is required to resolve the disk rotation curve (Mannings and Sargent 2000; Simon et al. 2000). The sample is biased to disks with strong CO emission that are found to have a large outer radius: 200–1,000 AU. However, smaller (and less massive) disks are detected around some heavily accreting TTSs, as BP Tau: the CO disk radius is ~120 AU and its mass ~ $1.2 \times 10^{-3}\,\mathrm{M}_\odot$ (Dutrey et al. 2003). All disks are found in Keplerian rotation with the exception of AB Aur that also shows a prominent spiral pattern in the optical and near infrared (Grady et al. 1999; Lin et al. 2006).

The main discriminating feature between disks around high and low mass PMS stars is the ratio between the disk and the stellar mass, M_d/M_*. In low mass stars $M_d/M_* < 0.1$, in massive B-type stars $M_d/M_* \leq 1$, and $M_d/M_* \gg 1$ in O-type stars. The stability and lifetime of high mass YSOs' disks is uncertain. Typically, the massive rotating structures observed in YSOs with luminosities ≥ $10^5\,\mathrm{L}_\odot$ have radii of 4,000–30,000 AU, masses of 60–500 $\mathrm{M}_\odot$, and rotation speeds of a few km s^{-1}. For these parameters, the accretion rate would be about $2 \times 10^{-3} - 2 \times 10^{-2}\,\mathrm{M}_\odot\,\mathrm{year}^{-1}$ (Zhang et al. 2005) corresponding to timescales for the whole disk depletion of 10^4 year, i.e., an order of magnitude smaller than the rotation period at the outer disk radius. This indicates that these very massive rotating structures cannot be centrifugally supported and should be considered as transient, nonequilibrium evolving structures; they probably host a stellar cluster. Most of the bona fide candidates to disks around high mass YSOs orbit about ~10 $\mathrm{M}_\odot$ stars, with luminosities typical of B-type ZAMS stars. In these objects, the estimated lifetime of the disks is about 10^5 year that it is comparable to the free-fall time of the mother molecular core. The most convincing disk around a high mass YSO has been detected in the Orion KL region through OH maser emission: IRAS 20126+4104 (Edris et al. 2005). The temperature law in the disk seems to follow $T(r) \propto r^{-3/4}$ and the rotation to be Keplerian (Cesaroni et al. 2005).

Identifying candidate disks around very massive protostars requires a careful selection of targets and tracers, to overcome the problems related to observations of massive YSOs. The most important of these are the large distance (a few kpc i.e. about ten times farther than the Gould's

Belt) and the confusion caused by the fact that massive stars form in rich clusters. In spite of the numerous attempts, no disks have been detected about early O-type stars (see Cesaroni et al. 2007 for a detailed analysis on possible observational biases).

3.3 Composition of Protostellar Disks

Disk composition is dominated by molecular hydrogen while the thermal properties of disks are controlled by dust that acts as the main coolant. A thin layer of atomic gas is also detected at the disk atmosphere caused by the photodissociation cascade activated by the stellar UV photons.

3.3.1 Dust

Dust composition and mixture is best investigated in the infrared spectrum of the PMS stars. The strong resonances of abundant dust species both O-rich (silicates either amorphous or crystalline) and C-rich (Polycyclic Aromatic Hydrocarbons or PAHs) are observed in the 8–13 μm range. The broad 9.7 μm amorphous silicate (Si-O stretching) feature dominates this wavelength regime and evolves from absorption in young, embedded sources, to emission in optically visible stars and to complete absence in debris disk systems both for TTSs and HAeBe stars (Furlan et al. 2006; Kessler-Silacci et al. 2005). The presence of PolyAromatic Hydrocarburs (PAHs) (6.2, 7.7, 8.6, 11.3 μm) has been reported in the spectra of only some TTSs (Geers et al. 2006).

A typical model of dust grain composition in protostellar disks consists of a mixture of three main components: small amorphous carbon grains, large silicate grains (in two basic compounds olivine and orthopyroxene), and silicate grains coated with "dirty ice." "Dirty ice" is mainly constituted of H_2O, CO, and other simple molecules though the exact composition is very uncertain and depends on the physical conditions and the local star forming history in the parent molecular cloud. The most abundant ice in protostellar disks is H_2O ice that plays a major role in the opacity of disks at temperatures below its vaporization threshold (Preibisch et al. 1993).

Grain growth in the dense protostellar disks modifies the size distribution with respect to that observed in the ISM[7] increasing a_{max} up to several microns and producing variations in the power index. Disk opacity is very sensitive to the fraction of dust grains with sizes comparable to the local thermal wavelength: $a \sim \lambda = 0.29 \, \mu\mathrm{m}/T(K)$. Ice and silicates behave like good dielectrics; following Mie theory, absorption and scattering efficiencies are weakly wavelength dependent if $a/\lambda > 1$ but below this value they drop rapidly to 0. As shown in ❯ *Table 6-1*, the fraction of the disk mass in silicates and water ice is about a 64% while refractory organics account for 25% of the total mass of the disk in dust. Strongly absorbing materials (with imaginary refraction index), such as iron or fractals made of highly conducting materials (e.g., graphite), represent a small fraction of the total dust mass of the disk (Pollack et al. 1994).

There are clear indications of dust evolution from the molecular cores to the protostellar disks. In addition to the coagulation of 0.1 μm to micron-sized dust grains that modifies the size distribution, dust observed in disks is crystallized resulting in an increasing fraction of crystalline silica, forsterite, and enstatite with respect to the amorphous pyroxene and olivine.

---

[7]The number density of grains of size, a, is given by $N(a) \propto a^{-3.5}$ with $a_{min} = 5 \times 10^{-3} \, \mu$m and $a_{max} = 0.25 \, \mu$m (Mathis et al. 1977).

⬛ **Table 6-1**

Dust grain species in protostellar disks[a]

Species	Bulk density (g/cm^{-3})	Mass fraction (M$_{specie}$/M$_{disk}$)
Metallic iron	7.87	1.26×10^{-4}
Olivine	3.40	2.51×10^{-3}
Orthopyroxene	3.49	7.33×10^{-4}
Troilite (FeS)	4.83	7.68×10^{-4}
Refractory organic	1.5	3.53×10^{-3}
Volatile organic	1.0	6.02×10^{-4}
Water ice	0.92	5.55×10^{-3}

[a]After Table 2 in Pollack et al. 1994. About 10% of the silicates were later found to be in crystalline form (Sargent et al. 2009), see text

In HAeBe stars, silicate emission provides evidence of stellar heating of the disk atmosphere in the inner ~10 AU. In fact, there is a very high fraction of crystalline dust in the central 1–2 AU around HAeBe stars. This decreases toward 2–10 AU but still is significantly higher than in the ISM, even at stages as early as 1 Myr, well before the onset of planet formation (van Boekel et al. 2004). This is surprising since the temperature in these areas of the disk is well below the glass formation temperature (about 1,000 K) but could be explained by chemical models of protoplanetary disks that include effects of radial mixing and local processes in the outer disk (Gail 2004). Crystalline silicate emission has been detected from TTSs; however, there is no evidence of a radial gradient in the mass fraction of crystalline silicates (Sargent et al. 2009).

As YSOs' disks evolve, their mid/far-infrared spectrum becomes more similar to that observed in comets. There is also a radial gradient in dust chemistry and in the grain size with large grains being more abundant in the inner disk.

3.3.2 Molecular Gas

H_2 is the main component of protostellar disks (the gas to dust mass ratio is ~100 and CO/H_2 ~ 7×10^{-5}) and does not freeze-out onto grains. Though the molecule is effectively photodissociated through absorption of UV radiation in the Lyman and Werner bands (912–1,100 Å range), H_2 self-shields efficiently against photodissociation. Unfortunately, the pure rotational lines in the infrared are intrinsically weak and difficult to detect. The strong electronic transitions at ultraviolet wavelengths are pumped by the stellar UV photons and are good tracers of the disk atmosphere and innermost region.

After CO and H_2, the most abundant gas molecules are: H_2O, OH, S_2H, HCO^+, CN, C_2H, CS, HCN, H_2CO, and DCO^+. The sensitivity of radio-interferometers has been too low to map their spatial distribution in disks. Simple molecules such as CO, ^{13}CO, HCO^+, CN, and HCN are detected from single dish observations. Line ratios indicate that the molecular emission arises from dense (10^6–10^8 cm^{-3}) and moderately warm ($T \sim 20-40$ K) intermediate height regions of the disk atmosphere between the midplane and the disk upper layer, in accordance with the predictions from models of disk chemistry. Molecular gas abundances are lower in the YSOs than in the molecular prestellar cores. This is caused by gas freezed out into dust grains in the cold midplane and molecules' photodissociation in the upper disk layers. CN is very strong in all disks. The CN/HCN abundance ratio toward the HAeBe stars is even higher than that

found in galactic photon-dominated regions, pointing out to the relevance of photodissociative processes in the upper layers of the disk. No CH_3OH has been detected to abundances 10^{-8}–10^{-9} with respect to H_2.

3.3.3 Disk Chemistry

Understanding disk chemistry requires to consider both gas phase and dust grain-surface processes. Dust grains are key ingredients in the disk chemistry since they control the degree of ionization in the most opaque areas of the disk; dust is an efficient electron donor for recombining ions and a sink for neutrals. At low temperatures ($T \simeq 10$ K) large molecules are stationary on the grain surface and grow by reaction with mobile species like hydrogen. However, as the temperature rises, diffusion and thermal evaporation produce desorption of the light species such as hydrogen, thus braking the hydrogenation-driven chemistry on the surface. Later, heavier compounds move from the grain surface to the gas phase. Desorption processes depend exponentially on the grain temperature, gas phase abundances, and chemistry; thus chemical modeling is very sensitive to the processing of the grain mantles. Surface reactions are compiled by Hasegawa et al. (1992) and Hasegawa and Herbst (1993) into the Ohio State University (OSU) gas-grain chemical model.

Gas phase reactions and their rate coefficients are available in the UMIST RATE06 database (Woodall et al. 2007) that includes about 420 species involving 13 elements: H, He, C, N, O, F, Na, Mg, Si, P, S, Cl, and Fe. Uncertainties in the chemical reaction rates (RATE06 contains about 4,800 chemical reactions) may lead to ill-determined gas columns by as much as a factor of ~4, for some species. This is mainly caused by the large uncertainties in about a hundred chemical reactions (Vasyunin et al. 2008). Species such as CO, H_3^+, H_2O, NH_3, N_2H^+, and $HCNH^+$ seem to be rather insensitive to these uncertainties while other relevant species such as CS, CO_2, H_2CO, CN, HCN, and HNC are sensitive to them. Further uncertainties in the chemical modeling of disks are introduced by the difficulties to identify the precise route to the formation of a given molecule, especially when dealing with large molecules that form both through gas phase and grain surface reactions. As an example, the theoretically derived abundance of $HCOOCH_3$ gas in class 0 YSOs (hot cores) through the gas-based formation route is roughly a third of the total abundance derived including both gas and grain routes (Garrod and Herbst 2006).
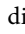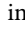
In general, chemical models of disk structure and evolution are developed with reduced sets of equations that are defined selecting only those species necessary to compute the abundances of the compounds under study. As an example, to determine the ionization degree of protostellar disks, Semenov et al. (2004) worked with a reduced network of chemical reactions selected according to a cutoff defined by the requested accuracy of the final model. The number of species included in the reduced chemical networks to study the disk ionization fraction ranged from four in the disk midplane at 1 AU from the star to some 50 at intermediate layers between the irradiated atmosphere in the opaque interior. The integration of gas phase and grain surface processes in chemical modeling of protostellar disks is hampered by the different nature of both processes. Gas phase chemistry can be simulated using rate equations; however, grain chemistry requires taking into consideration the availability of reacting particles in the grain. Some recent approaches have been taken introducing modified rate equations to grain surface reactions that include the probability of each reactant being available in the grain surface (Garrod et al. 2009).

Unfortunately, there is not yet a fully consistent disk model that solves for the chemical and dynamical structures simultaneously. As the chemistry of the disk evolves on timescales comparable to the dynamical timescale, this is a relevant source of uncertainty.

3.4 Disk Formation

During *Phase II*, accretion proceeds directly from the envelope of the molecular core onto the stellar embryo and the flattened structure that sets the seed of the disk. After roughly a free-fall time, material with negligible angular momentum has already been accreted onto the stellar embryo, the disk begins to develop and channels the mass flow onto the star.

The formation of an equilibrium disk requires that self-gravity balances gas pressure at any given point in the rotating disk. This balance is measured by the Toomre parameter,[8] Q, that must be larger than 1 for disks to remain stable. Disturbances on scales above $\Lambda_c = G\Sigma/\kappa^2$ are stabilized by the shear setting a maximum size of the unstable regions (Lynden-Bell and Pringle 1974). At smaller scales, instabilities develop, accompanied of local heating and angular momentum and mass transport.

Numerical simulations of the early gravitational collapse and disk/star differentiation are displayed in ❷ *Fig. 6-9* from Yorke and Bodenheimer (1999). Let us use them as a departure point to describe disk formation. Departing from an initial configuration $\rho(r) \propto r^{-2}$, a total mass of 2 M$_\odot$, and a specific angular momentum of ~10^{21} cm^2 s^{-1}, *Phase II* ends in about 10^5 years, just one free-fall time, since no hydromagnetic support is taken into account in this simulation. Afterward, the disk seed begins to grow radially. It is necessary to prescribe the radial transport of mass through the disk to the star to avoid mass accumulation in the disk, i.e., to evolve the flattened structure into an accretion disk. The pace at which matter flows onto the star is controlled by angular momentum conservation and thus, it is set by prescribing the angular momentum transport within the disk. This is often done by introducing the parameter α that scales the mass flow with the local sound speed in the disk. In this approach, transport within the disk is not a conservative process and a fraction of the gravitational energy is lost into disk heating and radiation. In the bottom panel of ❷ *Fig. 6-9*, it is shown how α needs to be modified for this particular simulation to keep the disk stable (according to Toomre's criterium). Major variations need to be introduced during the first free-fall time, after that α only needs to be varied mildly. Once transport is prescribed, the evolution of the disk during *Phase II* depends on the mass of the core (the larger the mass the earlier it ends) and on the initial specific angular momentum of the core (the smaller the angular momentum, the larger the amount of low angular momentum material available for direct accretion and so the duration of this phase). After the end of *Phase II*, the disk grows radially out to several thousands of AU and accretion shocks develop as the kinetic energy of the infalling material is released. The layered structure of the protostellar disk and the central force exerted by the star favors kinetic energy dissipation in two major steps. Firstly, an external shock front forms where the diffuse core material encounters the outer vertical edge of the disk. This material is later accelerated by the stellar gravitational field reaching highly supersonic velocities giving rise to the formation of a second inner shock front. The simulations represented in the figures are based on a simple treatment of angular momentum transport and ignore the presence of magnetic fields and the effect of outflows; as a result, after a little over three times the original free-fall scale, still 40% of the core mass is in the disk and the disk-to-mass ratio is 0.8, much larger than observed. In fact, values typically inferred from observations indicate that the disk-to-star mass ratio in low mass stars at protostellar stages is about 0.1 (Beckwith et al. 1990). Notice that

---

[8]Rotating, thin, gaseous disks are stable against gravitational perturbations if, $Q = c_s\kappa/\pi G\Sigma > 1$, where c_s is the sound speed, κ is the epicyclic frequency that measures the shear locally in the disk, G is the gravitational constant, and Σ is the surface density of matter (Toomre 1964).
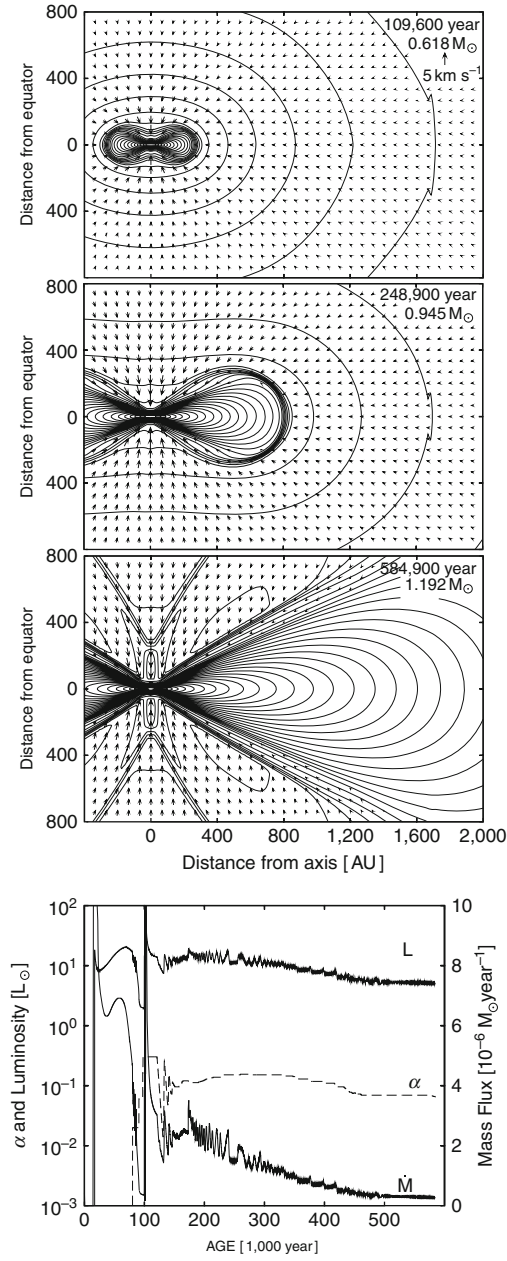
◻ Fig. 6-9

**Numerical simulations of the gravitational collapse of a 2$M_\odot$ from Yorke and Bodenheimer (1999).
(a) Density contours map and the velocity field are plotted at 0.56t_{ff}, 1.28t_{ff}, and 3.01t_{ff}, in the upper
panels. The initial angular velocity of the protostellar core is 5×10^{-14} s^{-1}. During disk evolution,
angular momentum transport is prescribed through the α formalism. (b) In the bottom inset, the
evolution of α needed to keep the disk stable and accreting during the gravitational collapse is
plotted, as well as the evolution of the luminosity (L) and the accretion rate ($\dot{M}$)**

if disks were to absorb directly all the angular momentum of the core, their radius would be $j^2/GM = 4.97\,\text{AU} \times 10^2 (j/10^{21})^2 (M/M_\odot)^{-1}$ and star formation would be a rather inefficient process since a fair fraction of the mass of the core would be kept stored in the disk. Angular momentum transport during disk formation is still an open problem.

3.5 Protostellar Disks and the α-Prescription Paradigm

The Toomre parameter is derived from pure hydrodynamical, linear theory; it cannot be applied to turbulent or magnetized disks. In 1973, Shakura and Sunyaev, showed that a simple prescription, the α-prescription, can be used to describe angular momentum transport and heating in disks. In this approach, disks are treated as a set of nested rings with surface density $\Sigma(r)$ that rotate at different angular velocities. The friction between adjacent rings generates a tangential stress $-\alpha\Sigma c_s^2$ that produces an inward flow of matter to the central object. The name of the prescription comes from the α parameter used to scale the stress with the local pressure. Each ring radiates through the disk face roughly as a blackbody with a temperature T(r) given by equating the gravitational energy dissipation rate to the blackbody flux:

$$T(r) = 2,100\,\text{K} \left(\frac{\dot{M}}{10^{-8} M_\odot \text{year}^{-1}} \right)^{1/4} \left(\frac{M_*}{M_\odot} \right)^{1/4} \left(\frac{r}{r_{in}} \right)^{-3/4} f(r)$$

where $\dot{M}$ is the accretion rate, $M_\odot$ and $R_\odot$ are the solar mass and radius, respectively, and $f(r) = (1-(r/R_*)^{-1/2})^{1/4}$. The magnitudes are scaled to typical values for TTSs: accretion rates of $10^{-8}\,M_\odot\text{year}^{-1}$, stellar masses of $1 M_\odot$, and inner disk radius, r_{in}, of about $3R_\odot = 0.014\,\text{AU}$. Henceforth, according to Wien's law, disk radiation should peak at the near infrared and, the higher the accretion rate, the higher the disk temperature should be. YSO's infrared SED is well fitted within this prescription that drove to the first classification of YSOs into class I, II, and III (Adams et al. 1987). The SED slope in the range 1–100 μm varies from $0 < s \le 1$ in class I sources, to $-2 \le s \le 0$ in class II sources, to $-3 < s \le -2$ in class III sources. In class I sources, the infalling envelope still has a non-negligible contribution to the infrared SED producing an excess toward lower energies and longer wavelengths. In class II sources, SEDs depend directly on the accretion rate following the α-prescription. Finally, the SED of class III sources is dominated by the reprocessing of the stellar radiation on the disks (see also ❯ Sect. 3.6).

In spite of this success, it is still unclear why the α-prescription works in protostellar disks. The α-prescription is tied to the definition of a kinematical viscosity, ν, such that $\nu = \alpha c_s(r)H(r)$ with $H(r)$ being the maximal scale of the flow circulation cell, considered to be of the order of the disk thickness (Lynden-Bell and Pringle 1974), in a disk analogue to the mixing length theory for stellar convection. In steady accretion disks, the radial mass flow is constant and the radial distribution of matter is prescribed by the disk viscosity, ν, as:

$$\Sigma(r) = \frac{1}{\nu(r)} \frac{\dot{M}}{3\pi} f(r)^4$$

with $\Sigma(r)$ being the disk surface density. However, hydrodynamical turbulence cannot feed this viscosity since Keplerian disks are stable to the Rayleigh criterion (angular momentum increases radially outward). Magnetohydrodynamical turbulence could play this role if the disk conductivity is high enough to allow the Magneto Rotational Instability (MRI) to set in and feed the turbulence cascade. To operate, MRI requires that the disk is magnetized so the field creates a stress, $-B_r B_\phi/4\pi$, that couples fluid elements at different radial distances from the star and forces them to exchange angular momentum (Balbus and Hawley 1991). The transfer of angular

momentum from the inner element to the outer element permits the inner element to move to lower orbits while the outer element moves to higher orbits. The magnetic tension acts like a spring that has as rest length the wavelength of the most rapidly growing mode. In principle, this scale corresponds to the length traveled by an Alfvén wave in one orbital period: $2\pi v_a(r)/\Omega$ where $\Omega(r)$ is the ring's angular velocity and $v_A = B/(4\pi\rho)^{1/2}$ is the Alfvén velocity. The finite thickness of the disk sets a vertical cutoff making the longest wavelength equal to $H(r)$, the disk thickness.

If the gravitational field is dominated by the star, the disk thickness can be readily derived as $H(r) = c_s(r)/\Omega(r)$ (or $H(r)/r = c_s(r)/(r\Omega(r))$) where $\Omega(r)$ is given by the third Kepler law[9]. As $c_s = \gamma k_B T/\mu m_H$, with γ the adiabatic index; μ the mean molecular weight, 2.4 as for a molecular H_2 disk; and m_H the mass of a hydrogen atom,

$$c_s(r) = 4.1 \,\mathrm{km\,s}^{-1} \left(\frac{\dot{M}}{10^{-8} M_\odot \mathrm{year}^{-1}} \right)^{1/8} \left(\frac{M_*}{M_\odot} \right)^{1/8} \left(\frac{r}{r_{in}} \right)^{-3/8} f(r)^{1/2}$$

and thus, a simple expression can be derived for $H(r)$ from the disk temperature law,

$$H(r) = 3.4 \times 10^9 \,\mathrm{cm} \left(\frac{\dot{M}}{10^{-8} M_\odot \mathrm{year}^{-1}} \right)^{1/8} \left(\frac{M_*}{M_\odot} \right)^{-3/8} \left(\frac{r}{r_{in}} \right)^{9/8} f(r)^{1/2}$$

This would set the basic scale for angular momentum transport at any given radius and thus, the efficiency of the mechanism.

Numerical simulations have been run to track down the nonlinear evolution of the MRI-driven cascade and the energy released into disk heating. The local physics of the disk is simulated in Cartesian boxes sheared by differential rotation where both tidal and Coriolis forces are taken into account, the so-called shearing box. Regardless of the initial field geometry and strength, even for weak field seeds, the simulations show that the magnetic and kinematic fluctuations transport angular momentum at a rate proportional to the magnetic pressure thus, the magnetic stress, $-B_r B_\phi/4\pi = \alpha_{\mathrm{mag}} \rho v_A^2$, with $\alpha_{\mathrm{mag}} \simeq 0.5 - 0.6$. This prescription is consistent with the α-prescription with $\alpha \sim 0.01$ (Hawley et al. 1995). The effects on the MRI evolution of the disk resistivity, the detailed analysis of the interaction between ions and neutrals in the fluid or the Hall currents have been studied in the shearing box approach (see Hawley 2009 for a recent review). Numerical simulations show that the turbulence depends on the sign of the magnetic field threading the disk and that quiescent and MRI-active regions may coexist in a complex dynamical structure that depends on the disk ionization degree.

The growth of MRI requires that the disk resistivity, η, satisfies $\eta \geq v_A H$. In turn, η depends on the electron fraction as: $\eta = 234 T^{1/2} \chi_e^{-1} \,\mathrm{cm}^2 \mathrm{s}^{-1}$. Thus, the MRI is approximately suppressed when,

$$\frac{v_A H}{\eta} = 7.4 \times 10^{13} \chi_e \alpha^{1/2} \left(\frac{r}{1\mathrm{AU}} \right)^{3/2} \left(\frac{T}{500\,\mathrm{K}} \right) \left(\frac{M_*}{M_\odot} \right)^{-1/2} \leq 1$$

i.e., when the electron fraction is roughly below 10^{-13} or the magnetic Reynolds number $R_M = v_A H/\eta < 1$ (Gammie 1996). This electron fraction depends on the main ionization sources and on the disk opacity to the environmental radiation. It is still unclear whether the MRI can be supported over the full disk extent or whether dead zones do exist. The high mass column of the dusty protostellar disks ($\geq 1,000\,\mathrm{g\,cm}^{-2}$) and the absence of strong internal sources of ionization may cause that dead and undead zones coexist. The ionization rates expected from the various possible contributors are shown in ❯ *Fig. 6-10* from Turner and

---

[9] $\Omega(r) = (GM)^{1/2} r^{-3/2} = 2\pi years^{-1} (M/M_\odot)^{1/2} (r/1\mathrm{AU})^{-3/2}$.
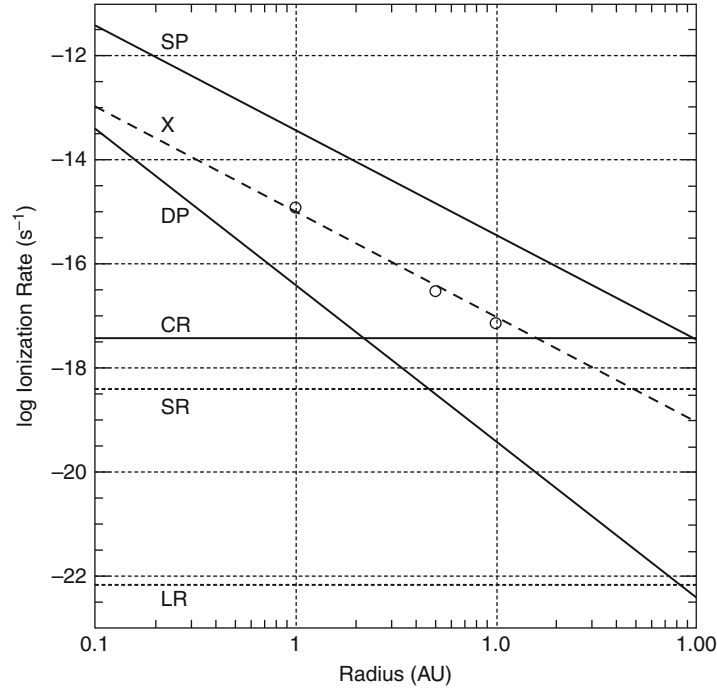
□ Fig. 6-10

**Ionization rates at column 8 g cm^{-2} versus distance from the star from Turner and Drake (2009).
The *dashed line* shows the contribution of stellar X-rays, and the *dotted lines* the decay of the short-
lived (*upper*) and long-lived (*lower*) radionuclides. Among the three *solid lines*, the uppermost is for
stellar energetic particles, the steepest shows the disk coronal particles, and the *horizontal solid line*
is for interstellar cosmic rays. Large surface density is assumed and only radiation striking the top
of the disk is included on the diagram. *Circles* indicate the results of the Monte Carlo X-ray transfer
calculation by Igea and Glassgold (1999), scaled to a stellar X-ray luminosity of 2 × 10^{30} erg s^{-1};
in these simulations the disk is illuminated from above – the source of energy is located at ~10$R_\odot$
above the disk on the axis. The disk coronal particle estimate corresponds to a fraction of 10^{-4} of
the energy released by mass accretion at a rate of 10^{-8}M$_\odot$year^{-1}**

Drake   (2009)
for a uniform gas column of 8 g cm^2 as a function of the distance to the star. Cosmic ray prop-
agation provides uniform ionization rates across the disk that can be enhanced by as much as a
factor of a thousand in the proximity of a supernova remnant. The decay of radionuclides' con-
tribution is negligible even for short-lived species (primarily Al^{26} with half-life 0.717 Myr). The
main source of ionization within the inner 100 AU is the radiation released in the high-energy
processes associated with the star and the disk–star interaction region that penetrates through
the disk atmosphere toward the midplane.

Thus, the ionization degree of disks depends on their vertical structure that it is still poorly
constraint (see ❯ Sect. 3.6.2). There are, however, indications that turbulent mixing may be
able to prevent the formation of dead zones (Ilgner and Nelson 2008).

3.5.1 The α-Prescription and Angular Momentum Transport by Gravitational Waves

Once massive disk-like structures form (in 1–3 free-fall times), they are especially prone to gravitational waves and instabilities. Gravitational waves can effectively transport angular momentum in a conservative manner, without dissipation, and they are a global phenomenon that propagate over the whole disk as opposite to the α-disk model that is based on the properties of turbulence, i.e., on the *local* dissipation of disturbances.

Gravitational instabilities and waves are a well-studied mean for angular momentum transport via tidal torques (see Lin and Papaloizou 1996 for a review on angular momentum transport mechanisms in disks). The simplest modes are one-armed spirals built from a progressive tilted sequence of elliptical orbits (Adams et al. 1989); however, they do not play a dominant role in YSOs' disks (Durisen et al. 2007). In general, non-axisymmetric disturbances grow as multi-armed spirals that become unstable for $Q < 1.5$ (see ❯ *Fig. 6-11*). Dissipation is driven by compression and subsequent heating/cooling of the gas that can be enhanced by shocks driving to a *local* dissipation of energy. Nonlinear wave coupling produces a wide spectrum of waves resulting in a cascade from single gravitational modes to a broad variety of wavelengths and arms. Disks evolving under self-gravity tend to keep around $Q \simeq 1$ (Laughlin and Bodenheimer 1994) and anomalous energy transport terms related with the gravitational shear can become negligible supporting the use of the α-prescription to track the radial angular momentum transport (Balbus and Papaloizou 1999). In this case a gravitational turbulence (or gravito-turbulence) α_g parameter can be defined. As an example, the tuned α-prescription used to treat gravitational collapse in ❯ *Fig. 6-9* is set to keep Q between 1.3 and 1.5 assuming that the disk evolves toward marginal gravitational instability and maintains it during its evolution. This gravitational α or α_g needs to be submitted to rapid variations during the beginning of the gravitational collapse due to the rapid compression; however, after this period α_g stabilizes around 0.05 for a solar mass core.

The α_g parameter can also be used to evaluate the disk stability against fragmentation; gravitational waves can drive local compression that for a given disk opacity renders the disk unstable producing disk fragmentation into protoplanets or brown dwarfs (see Goodwin's chapter). In thermal equilibrium, α_g can be evaluated from the disk cooling time, τ_c, as:

$$\alpha_g = \frac{4}{9\gamma(\gamma-1)\Omega\tau_c} \qquad (6.1)$$

(Gammie 2001). Numerical simulations by Rice et al. (2005) suggest that only if $\alpha_g < 0.06$ angular momentum transport is viable without driving to disk fragmentation.

In general, the disk dispersal timescale would be around 10^7 years if only gravitational instabilities are considered; however disk dispersal timescales derived from the observations are significantly shorter ~5 Myr (Haisch et al. 2001). MRI and gravitational instabilities have complementary properties and their joint action, together with the disk irradiation and outflow, could explain the main observed properties of protostellar disks.

3.6 Disk Structure: The Effect of Stellar Irradiation

X-ray and, especially, high-energy particles are able to penetrate deep in the disk releasing their energy within the disk interior. Photoionizing ultraviolet radiation is rapidly absorbed at the
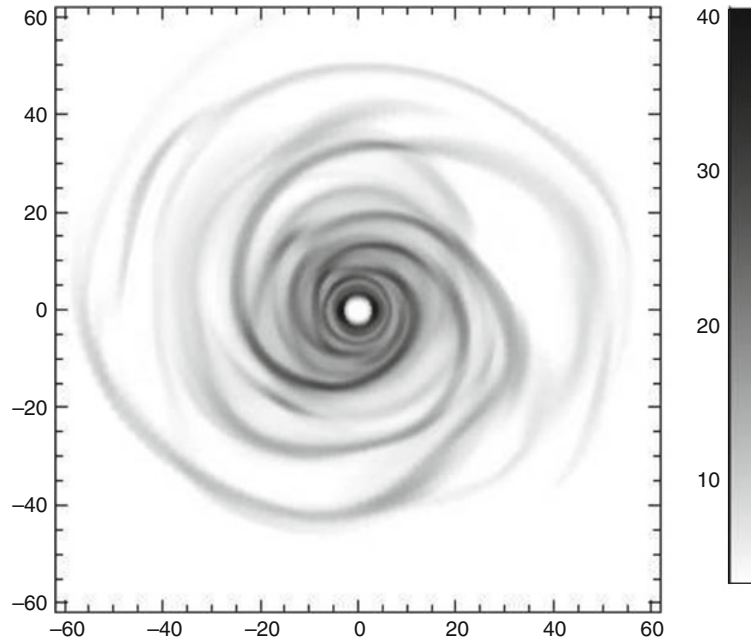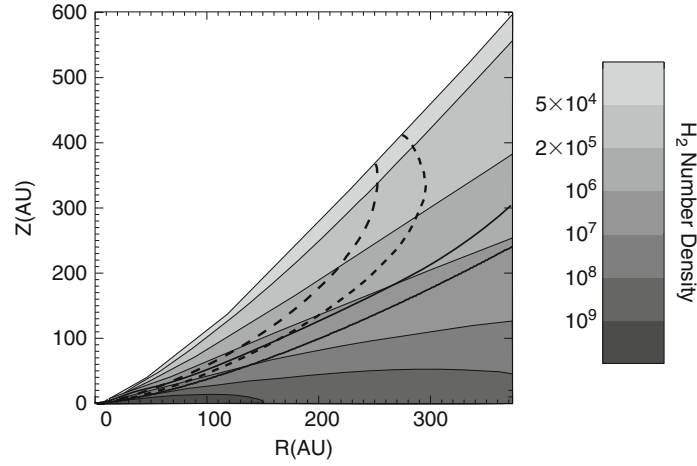
⬛ Fig. 6-11

Shocks and spiral waves **from numerical simulations of gravitational instabilities in YSOs' disk (after Mejía et al. 2005). The** *grayscale codes* **the effective temperature of the gas in a disk undergoing gravitational instabilities that has reached an asymptotic state of thermal self-regulation. The mass of the disk is 0.07 M$_\odot$ and it is orbiting around a 0.5 M$_\odot$ star**

surface by the two main compounds of disks: dust and gas. Dust grains efficiently absorb UV photons through the photoelectric effect, gas particles do it through the resonance transitions of both molecules and atoms. A PhotoDissotiation Region (PDR) forms at the surface that has its own dynamics and carves the disk surface producing photoevaporative flows. The penetration of the ionizing radiation toward the disk midplane depends on the disk opacity that is dominated by dust grains at temperatures below 1,500 K (i.e., over most of the disk volume). According to the penetration of the stellar high-energy radiation protostellar disks are divided into three basic layers (see ❯ *Fig. 6-12*):

- *Dense midplane*: which is opaque to both X-ray and UV radiation and is ionized primarily by cosmic ray particles.
- *Intermediate layer*: which is opaque to UV radiation. The bottom of this layer will be defined by the height at which fractional ionization begins to grow due to the stellar X-rays photons.
- *Atmosphere*: which is transparent to the stellar UV radiation. The bottom of this layer will be defined by the height at which fractional ionization begins to grow due to the stellar UV photons.

The thickness of these layers and the location of the frontiers depends on the details of the protostellar disk model: irradiation field, dust opacity, density, and temperature laws in the disk.

◨ Fig. 6-12

Vertical structure of YSOs disks. The *gray levels* mark the number density of H_2 molecules in the disk from the D'Alessio et al. (1998) model. The *thick lines* trace the scale height of the disk for a standard (nonirradiated) α disk – *bottom line* – and for an irradiated disk – *top line*. The *dotted lines* mark the penetration of the UV (1,000 Å) and optical (3,400 Å) radiation from the central source into the disk. Radiation impinging at the disk surface drops by a factor of 10^{-6} at the location of the lines: *top* (UV), *bottom* (optical) (from Van Zadelhoff et al. 2003)

Solving the full structure of the disk is thus, a complex problem since many different processes are coupled.

3.6.1 YSOs' X-ray and UV Radiation Field

The observed X-ray luminosity of YSOs is on average about 10^{30} erg s^{-1} and the energy distribution is well fitted by the thermal radiation of optically thin plasmas at temperatures of ~5–30 MK (see i.e. Guedel 2008); for comparison the Solar X-ray luminosity is about 10^{27} erg s^{-1} and the plasma temperatures 1–2 MK. In class I and II YSOs, the X-ray spectrum often shows the contribution of two unrelated components subjected to very different absorption: a soft component from a cool (1–2 MK) plasma that is barely absorbed and a much harder component (10–30 MK) subjected to about ten times higher absorption. X-ray-induced iron Kα emission from the disk has been detected from some YSOs, tracing directly the effect of X-ray irradiation on the disk surface (Giardino et al. 2007).

The main effect of X-ray photons is to ionize atomic hydrogen that ends shielding the disk to the penetration of the X-ray radiation. Also, X-ray-induced photons produce the desorption of formaldehyde (H_2CO) from grain surfaces. Chemical evolution models show that this process is fundamental for the disk ionization (and coupling to the magnetic field) since HCO$^+$ becomes the dominant ion in the intermediate layer of the disk in timescales comparable to the disk evolution timescales (about 10^6 years).

The UV luminosity of YSOs is ill determined. During the early phases heavy dust extinction prevents measuring directly the UV radiation field and only indirect measurements are available based on the chemical modeling of disks. The radiative UV output from massive YSOs (O to A spectral types) can be modeled using blackbody spectral energy distributions but the UV spectrum of low mass YSOs is dominated by the extended magnetosphere/atmosphere and it is poorly constraint from the observations. Typically, line fluxes of TTSs are a factor of 50 stronger than their main sequence analogues (see Gómez de Castro 2009 and references therein). Accretion also contributes to the UV excess of TTS and HAeBe stars (see ❷ Sect. 4).

UV radiation interacts strongly with matter in the disk. H_2 dissociates through absorption in the Lyman and Werner bands (912–1,100 Å range). As H_2 is the main component of protostellar disks, its response to the UV radiation field etches the surface of the disk. Unfortunately, very few observations are available of TTSs (Herczeg et al. 2002; Wilkinson et al. 2002) and Herbig stars (Martin-Zaidi et al. 2008) in the 912–1,100 Å range. The absorption of UV photons is followed by UV and IR fluorescence that has been detected from the disk of several TTSs (Herczeg et al. 2004). Only about 15% of the photons lead to H_2 photodissociation. The neutral gas is ionized by the Lyman continuum radiation that heats it to some 10,000 K surpassing the escape velocity from the disk surface (see ❷ Sect. 3.8).

UV photons are also absorbed/scattered by the dust and dust grains get charged through the photoelectric effect releasing high-energy electrons that heat collisionaly the plasma. The kinetic energy of the photoelectrons depends on the hardness of the illuminating UV spectrum since the dust absorption cross section covers a broad spectral range; dust extinction peaks at about 750 Å and declines toward X-rays (Laor and Draine 1993) with a characteristic absorption cross section in the Lyman continuum as $\sim 0.61 \times 10^{-21}$ cm^{-2}. The photoelectric charging of the dust grains produces a population of secondary fast photoelectrons in the atmosphere of the disk whose characteristics depend on the illuminating radiation field. In ❷ *Fig. 6-13a*, the most characteristic ionizing spectra in the YSO's environments are plotted. Blackbodies at 50,000 and 10,000 K represent roughly the energy distribution of O-type and A-type YSOs. The fit to the galactic UV background based on early UV missions (Draine 1978) is also plot. Finally, a high-energy spectrum has been built by assuming that the X-ray radiation of the TTSs is produced by magnetic reconnection in a clumpy corona. The interaction of the X-ray photons with the dense ($\sim 10^9$ cm^{-3}) clumps produces the UV spectrum plotted. The charging profiles of the dust grains are shown in ❷ *Fig. 6-13b*.

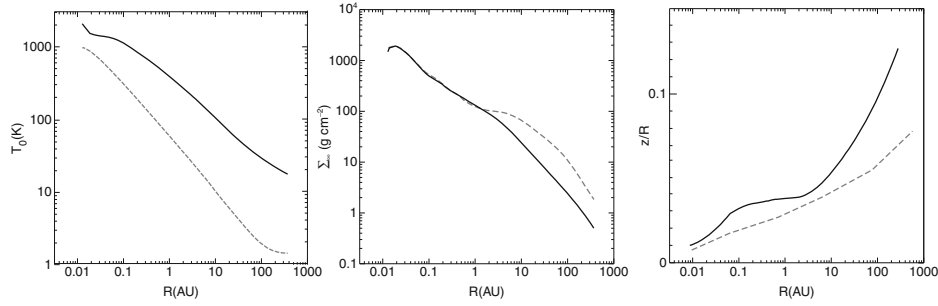### 3.6.2 The Vertical Structure of Disks

The innermost region of the YSO's disk is heavily disturbed by the interaction with the stellar magnetosphere in TTSs (see ❷ Sect. 4) and by the stellar radiation field in HAeBe stars. Further out, disks can be treated as rather simple structures. In the absence of dead zones, most of the accretion energy is expected to be released at the disk midplane that cools mainly by dust continuum radiation in the infrared range. At the same time, the disk is heated from above (from the atmosphere to the midplane) by the high-energy radiation produced in the inner region (star, magnetosphere, inner outflow).

In a first approach, D'Alessio et al. (1998) computed the vertical structure of an stationary α-disk irradiated by a TTS with effective temperature 4,000 K. Cosmic rays and radioactive decay were also considered as sources of disk ionization. At every given radius, the disk is treated as a stratified, plane-parallel atmosphere. Viscous dissipation in the α-disks occurs locally, and
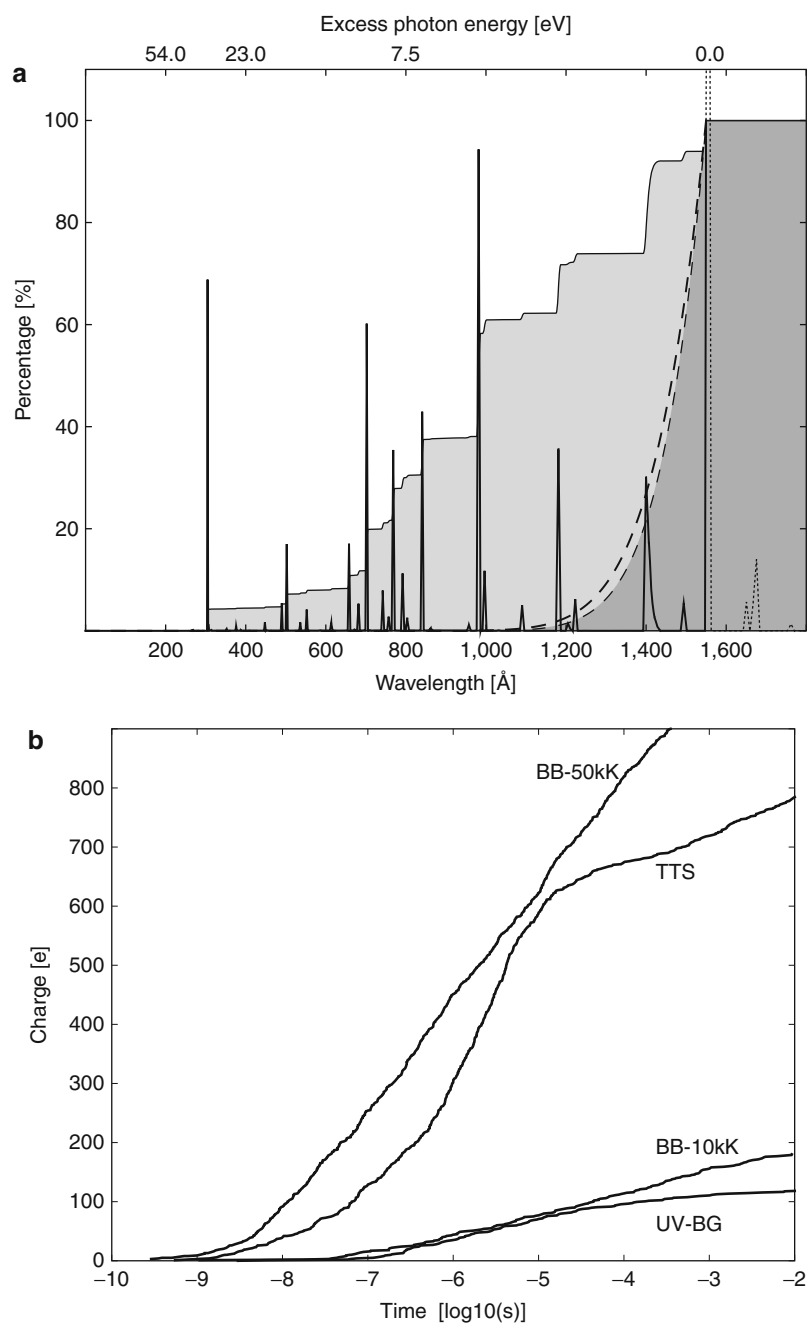
◘ Fig. 6-13

Response of dust grains to typical UV radiation fields in the YSO's environments. (a) UV radiation fields normalized to the same total energy of a 50,000 K blackbody (*shadowed continuous line*), a 10,000 K blackbody (*dark shadowed dashed line*), the UV background (*dashed line*), and the hard TTS spectrum (*continuous line*). (b) Evolution of the grain charge with time at 1 AU from the star (from Pedersen and Gómez de Castro 2011)
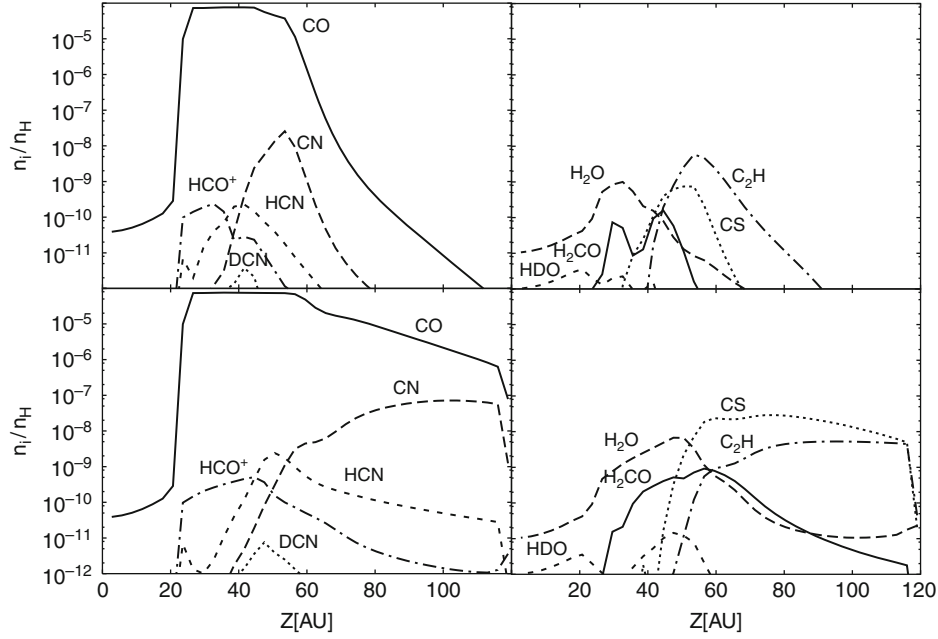
◨ Fig. 6-14
Vertical structure of an irradiated disk (*solid lines*) compared with a standard accretion α-disk (*dashed lines*) for an accretion rate of $10^{-8}\,M_\odot\,\mathrm{year}^{-1}$ onto a $0.5\,M_\odot$ star (from D'Alessio et al. 1998). ***Left panel*: Temperature at the disk surface, *T*, for an irradiated disk (*solid line*) and a nonirradiated disk (*dotted line*). *Central panel*: Radial distribution of surface density of an irradiated (*solid line*) and a nonirradiated (*dashed line*) disk model. *Right panel*: Characteristic height as a function of R**

the energy rate generated per unit volume is computed assuming α = 0.01 and an accretion rate of $10^{-8}\,M_\odot$ year^{-1}. Stellar photons are assumed to enter in the disk at grazing angles as in a flared disk.[10] A fraction of the stellar radiation is scattered at the upper boundary of the disk creating a diffuse field at the disk surface; it is assumed that gas and dust are thermally coupled in the disk.

With this provision, this simple model already shows that irradiation from the central star is the dominant heating agent farther than some 5 AU. As a result the temperature distribution of the disk changes from $T(r) \propto r^{-3/4}$ to $T(r) \propto r^{-1/2}$ and the disk becomes less dense than in the purely viscous case. In this model, the disk temperature has a vertical inversion caused by the properties of the dust opacity. Dust is more opaque to the optical stellar spectrum than to the infrared radiation produced by itself to release the viscous heating. This creates a superheated layer above the disk photosphere where most of the stellar radiative energy is spent into dust heating. In ❷ *Fig. 6-14*, the temperature law, surface density, and scale height are compared for irradiated and nonirradiated accretion disks.

The D'Alessio et al. (1998) model has been extensively used as a baseline to study disk chemistry and ionization state. For instance, Van Zadelhoff et al. (2003) used the density and temperature structure of the disk derived from 1-D modeling to compute in more detail the propagation of UV radiation into the disk interior. From this, the vertical distribution of molecules is computed for different disk radii and stellar irradiation fields. As shown in ❷ *Fig. 6-15*, the vertical distribution of some molecules is very sensitive to the UV irradiation field. In the absence of a significant UV radiation field, the CO photodissociation rate becomes small and the molecule survives further in the disk atmosphere. As a result, the column densities of abundant radicals such as CN or C_2N decrease in the inner regions due to the smaller supply of atomic carbon. The chemical timescale is very short in the disk midplane since adsorption on dust grains dominates the chemistry ~ 100 yr (10^8 cm$^{-3}/n_H$); however, in the intermediate layer steady state is

---

[10]In disk modeling, it is often assumed that the stellar photons enter the disk surface at grazing angles given by $\phi \simeq h_*^{eff}/r + dH/dr - H/r$, where h_*^{eff} is the effective height of the stellar radiation field over the disk midplane, often taken as $0.4R_*$.

◨ Fig. 6-15

Vertical distribution of molecules at R = 105 AU and t = 1 Myr structure of an irradiated disk (after Van Zadelhoff et al. 2003). *Top*, **the disk is assumed to be irradiated by the spectrum of a TTS from 1,000 to 10,000 Å.** *Bottom*, **the disk is assumed to be irradiated with Draine's (1978) spectrum**

reached in 10^4–10^5 years for many organic molecules and this timescale is significantly larger than the UV flux variability timescales (days to years).

The ionization structure of the disk has also been calculated based on this simple 1-D model (Semenov et al. 2004) who found a dead region between 2 and 20 AU where the ionization fraction is not high enough to keep the gas coupled to the magnetic field. In this area, MRI would not grow keeping the disk midplane cooler than in the standard α-model and preventing mass transport. This raised concerns on the applicability of the MRI to the cool and dense protostellar disks and drove to the development of new disk models that take into account vertical mixing between the midplane and the irradiated disk surface. Ilgner and Nelson (2008) have made use of a simplified chemical model for the gas phase chemistry to code in the ionization fraction evolution in a sheared box–based model of a magnetized accretion disk. The chemical model is based on charge exchange reactions between H_2 and Mg (Oppenheimer and Dalgarno 1974) that are well suited to follow the electron fraction in the disk (Ilgner and Nelson 2006). For a fiducial temperature of 100 K, the charge transfer reaction ($H_2^+ + Mg \rightarrow H_2 + Mg^+$) occurs at a rate that is about 1% of the H_2^+ recombination rate. As the recombination rate of Mg^+ is five orders of magnitude lower than of H_2^+, a Mg-rich gas will sustain better a higher ionization fraction favoring MRI development. The model does not take into account the ionization of the disk surface by UV radiation and considers a Mg abundance slightly below the solar. With these provisions, the numerical calculations led to a fully turbulent disk with no dead zones.

A full disk modeling including the MRI cascade to turbulence, disk irradiation, and the microphysics of the dissipative processes is yet to be done.

3.7 Disk Stability

Some TTSs are observed to suffer nova-like outburst. They are named FUOrs as the proto-type of the class: FU Ori. During the outburst, the system brightens by several magnitudes (≥ 4 magnitudes in V) followed by a decade-long fading (see Abraham et al. 2004 for a compilation of these sources). The transport rate typically rises to $10^{-4} M_\odot$ year^{-1} during the outburst (Hartmann and Kenyon 1996).

Disk emission dominates at all the wavelengths during outburst suggesting that YSOs' disks are prone to strong instabilities. Disk instability triggering can be intrinsic to the disk or extrinsic. Extrinsic instabilities are driven by the close passage of nearby stars or the presence of a companion in a wide, highly eccentric orbit. Accretion disks may also render unstable by thermal instabilities and frontier instabilities related with the coexistence of two transport mechanisms (MRI and gravitational waves) in the disk.

Thermal instabilities are driven by strong enhancements of the disk opacity as the temperature rises locally. The α-prescription relates the accretion rate with the local disk temperature; thus, as the temperature rises, the effective local mass flux also increases and the hot regions begin to propagate radially through the disk on a timescale $\tau_p \sim r/\alpha c_s \sim$ 5 year$(r/0.1\,\mathrm{AU})/(c_s/10\,\mathrm{kms})^{-1}$ years for $\alpha = 10^{-2}$. During the outburst, the ionized regions deplete on the viscous diffusion timescale, $\sim r^2/\nu \sim (\Omega/c_s)\tau_p$, that is about ten times the propagation timescale. The opacity of protostellar disks is not a smooth function of the temperature but shows strong jumps between the dust melting point and the onset of scattering by atomic hydrogen as the main source of opacity. After dust grains melting (above ~1,500 K), the opacity drops by about four orders of magnitude; however as the temperature increases from 2,000 to 10,000 K the opacity rises by eight orders of magnitude(!) by the onset of hydrogen scattering. Thus, a variation on the accretion rate enough to drive the inner disk to the dust melting point have strong effects on the disk structure. Bell and Lin (1994) developed the first models for this process based on work done for outburst generation in accretion disks within cataclysmic variables. However, the model requires very high accretion rates and very low $\alpha (\simeq 10^{-4})$ to reproduce the observations that are unusual for protostellar disks (see Bell and Lin 1995; Turner et al. 1997 for later developments).

Another unstable regime can be built in the disk if there is a physical boundary separating an MRI-dominated accretion flow in the inner disk from a gravitational instability–dominated flow in the outer disk. Material could pile up at this border and cause the temperature in the inner disk to rise to remain gravitationally stable (to keep $Q \sim 1$). Once hot enough, the increase of the ionization fraction would onset the MRI producing an accretion outburst (Armitage et al. 2001).

3.8 Disk Evolution

Two competing scenarios have been proposed to drive disk evolution:

- *Cool evolution* driven by gravity
- *Hot evolution* that takes into account the effect of the stellar radiation field into disk photoevaporation
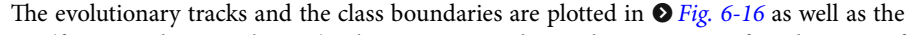
Cool evolution is driven by the exhaust of remnant material in the molecular core to feed the disk with fresh gas for accretion. Typical models follow the evolution of the rotating protostellar core

under self-gravity with some simplifying assumptions to make the problem tractable (Yorke and Bodenheimer 1999; Yorke and Sonnhalter 2002; Young and Evans 2005). The energy sources are identified: star (accretion and deuterium burning), disk (accretion, direct infall of gas from the envelope), and star–disk boundary layer. Radiative transfer within the dusty envelope is computed and from that, the main observables are determined. The two main observables are the so-called bolometric temperature of the YSO and its bolometric luminosity. The bolometric temperature is defined as the temperature of a blackbody with the same flux-weighted mean frequency as the source:

$$T_{\mathrm{bol}} = 1.25 \times 10^{-11} \frac{\int_0^\infty \nu S_\nu d\nu}{\int_0^\infty S_\nu d\nu}$$

T_{bol} tracks the evolution of the SED, from the heavily weighted to the far infrared SEDs of class 0 YSOs, to the optically weighted SEDs of class III YSOs, already very close to the zero age main sequence (ZAMS). The boundaries of the YSOs' classes were redefined according to T_{bol} (Chen et al. 1995) as follows:

Class 0: $T_{\mathrm{bol}} < 70\,\mathrm{K}$
Class I: $70\,\mathrm{K} \leq T_{\mathrm{bol}} \leq 650\,\mathrm{K}$
Class II: $650\,\mathrm{K} < T_{\mathrm{bol}} \leq 2,800\,\mathrm{K}$
Class III: $T_{\mathrm{bol}} > 2,800\,\mathrm{K}$

The evolutionary tracks and the class boundaries are plotted in ❷ *Fig. 6-16* as well as the ZAMS (from Dunham et al. 2010). The 1,024 YSOs detected in a major infrared survey of star forming regions (Evans et al. 2009) is overplotted. The evolutionary tracks for $1\,\mathrm{M}_\odot$ and $3\,\mathrm{M}_\odot$ protostellar cores are represented for two families of models, Young and Evans (2005) and Myers et al. (1998), where accretion rates are prescribed to decrease exponentially with time. The low luminosity of class 0 sources evidence unexpectedly low accretion rates $\leq 10^{-6}\,\mathrm{M}_\odot$ year^{-1} suggesting that accretion could be episodic in nature since the very early phases.

Hot evolution: the impact of the stellar radiation field into disk evolution is taken into account. UV radiation is very efficient at etching the disk surface by producing a thermal flow. The tenuous gas in the disk atmosphere is ionized and heated to temperatures of $\sim 10^4$ K. The thermal velocity of the gas reaches typically $V_{th} \sim 11.4\,\mathrm{km\,s^{-1}}$ leading to a slow photoevaporative flow at radii, r_s, where the thermal speed surpasses the escape velocity from the disk surface: $r_s = 15.6\,\mathrm{AU}\,\frac{M_*}{M_\odot}\,(V_{th}/11.4\,\mathrm{km\,s^{-1}})^{-2}$. When the dynamics of the process is analyzed, it is shown that the flow crosses the sonic point if $r > 0.1 r_s$ (Font et al. 2004). The mass-loss rate in photoevaporative outflows can be roughly estimated as:

$$\dot{M} \sim 4 \times 10^{-10}\,\mathrm{M}_\odot\mathrm{year}^{-1} \left(\frac{C_{\mathrm{Lyc}}}{10^{41}} \right)^{1/2} \left(\frac{M_*}{M_\odot} \right)^{1/2}$$

where C_{Lyc} is the count rate in the Lyman continuum (Hollenbach et al. 1994). However, as soon as hydrogen recombines, the flow itself may shield the upper layers of the disk atmosphere to the UV radiation. A measure of the opacity of the photoevaporative flow to Lyman continuum photons can be given by the parameter:

$$\Psi = \frac{\alpha_B C_{\mathrm{Lyc}} \delta r \phi}{4\pi r^2 V_{th}^2} = 1.1 \times 10^2 \frac{C_{\mathrm{Lyc}}}{10^{41}} \frac{\delta r}{1\mathrm{AU}} \left(\frac{r}{1\mathrm{AU}} \right)^{-2}$$

where α_B is the case B hydrogen recombination coefficient and δr is the thickness of the photoevaporative flow in the direction of radiation propagation (Bertoldi 1989). Significant photoevaporative flows require $\Psi \gg 1$.
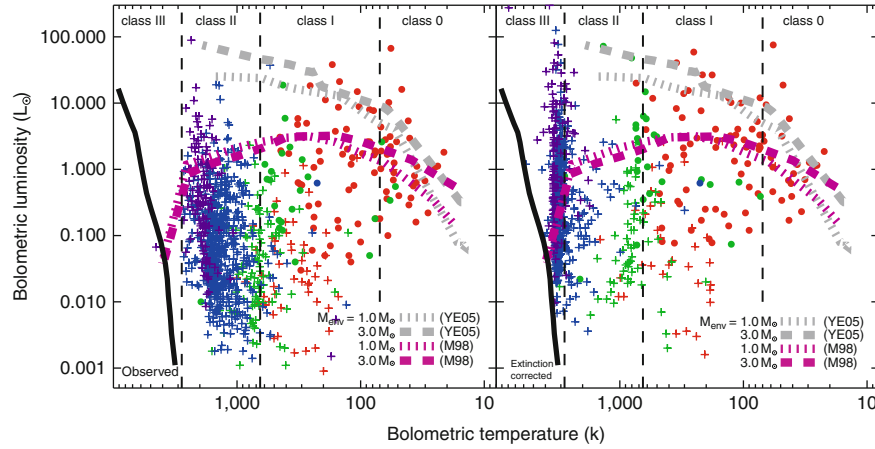
◧ Fig. 6-16

Cool evolution of YSOs represented in a bolometric luminosity versus bolometric temperature diagram (after Evans et al. 2009). Class I YSOs are plotted in *red*, Flat in *green*, Class II in *blue*, and Class III in *purple*. *Filled circles* indicate sources associated with envelopes as traced by millimeter continuum emission, while *plus signs* indicate sources with no such associations. The *thick lines* are model tracks for initial core masses of 1.0, and 3.0 M from Young and Evans (2005) and Myers et al. (1998) marked in *gray* and *purple*, respectively. The *vertical dashed lines* show the boundaries between classes, as defined by Chen et al. (1995). The heavy *dashed line* on the left is the ZAMS D'Antona and Mazzitelli (1997) from 0.1 to 2 M$_\odot$. Data are represented without and with extinction correction in the *left* and *right panels*, respectively

Once the irradiation field photoevaporates the inner disk, viscous spreading tends to move matter to this area accelerating disk dissipation. The evolution of disks is modeled through the diffusion equation for the disk surface density, $\Sigma(r, t)$:

$$\frac{\partial \Sigma}{\partial t} = \frac{3}{r} \frac{\partial}{\partial r} \left(r^{1/2} \frac{\partial}{\partial r} \left(\nu \Sigma r^{1/2} \right) \right) + \frac{d\Sigma_w}{dt}$$

where the vertical structure is neglected and an extra term is added to the initial Lynden-Bell and Pringle (1974) formulation to account for the impact of photoevaporative flows. As shown in ❯ *Fig. 6-17* from Alexander et al. (2006), there is a rapid transition in the disk structure at ~6 Myrs. Once the inner hole is excavated the spread of the inner cavity drives to full disk photoevaporation in few 10^4 years.

4 PMS Evolution: The Outflow

Outflow is the first signature of star formation however, no theory anticipated it prior to the discovery of the bipolar molecular outflow from L1551 by Snell et al. 1980. A decade later, Andre et al. (1990) detected the VLA 1623 outflow from a Class 0 YSO, pointing out that bipolar outflows are ejected as early as during *Phase II*. The collimation and mechanical power of the
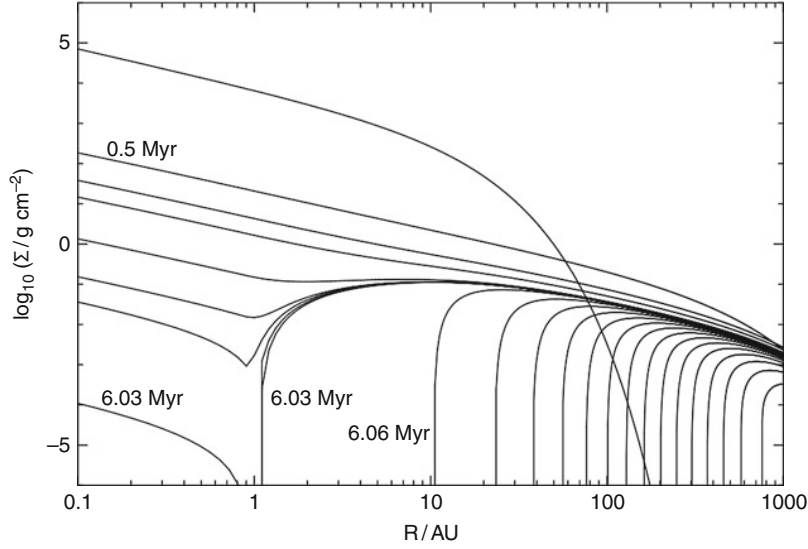
◼ Fig. 6-17

Hot evolution of YSOs' disks **after Alexander et al. 2006. Photoevaporation drills an inner hole in the disk in roughly 1 Myr. The curves represent the evolution of the disk surface density, from an initial value of ~ 10^5 g cm^{-2} in the inner border of the disk to a final state with ~ 10^4 g cm^{-2}. Notice that in 6 Myr, the area at R = 1 AU is evacuated**

outflows decreases as stars approach the main sequence and protostellar disks evolve into debris disks as shown in ❯ *Fig. 6-18*.

The tracers of the outflows depend on the degree of evolution of the parent source. Flows from young class 0/I sources often contain molecules such as H_2, CO, and SiO. Later on, they tend to be dominated by HI and low-ionization metals that show as prominent large-scale jets detected at optical wavelengths ([S II], [N II], or H_α lines). Mass-loss rates decline from ~10^{-6} $M_\odot$ year^{-1} in the class 0 YSOs, to ~10^{-8} $M_\odot$ year^{-1} in class I, and ~10^{-10} $M_\odot$ year^{-1} in class II. Typically, the outflow mass-loss rate is about a 10% of the accretion rate and the velocity about few hundred km s^{-1}.

The main mechanical properties of bipolar outflows have been recently redetermined from the large data base of known CO outflows (Wu et al. 2004):

- The mass carried out by the outflows, $M_{w,CO}$, correlates strongly with the bolometric luminosities of the outflow powering source, L_{bol}. The flow mass increases with the luminosity as a power law: $\log M_{w,CO} = (-1.04 \pm 0.08) + (0.56 \pm 0.02) \log L_{bol}$.
- The mechanical force needed to accelerate the outflow ($F_{w,CO} = \dot{M}_{w,CO} V_{w,CO}$) is larger than the radiative force from the parent YSO: L_{bol}/c. There is, however, a clear correlation between mechanical and radiative power from the source: $\log F_{w,CO} = (-0.92 \pm 0.15) + (0.65 \pm 0.04) \log L_{bol}$.

These relations (see ❯ *Fig. 6-19*) indicate that accretion, the major source of energy during star formation, powers the formation of outflows. Moreover, these relations hold from low mass
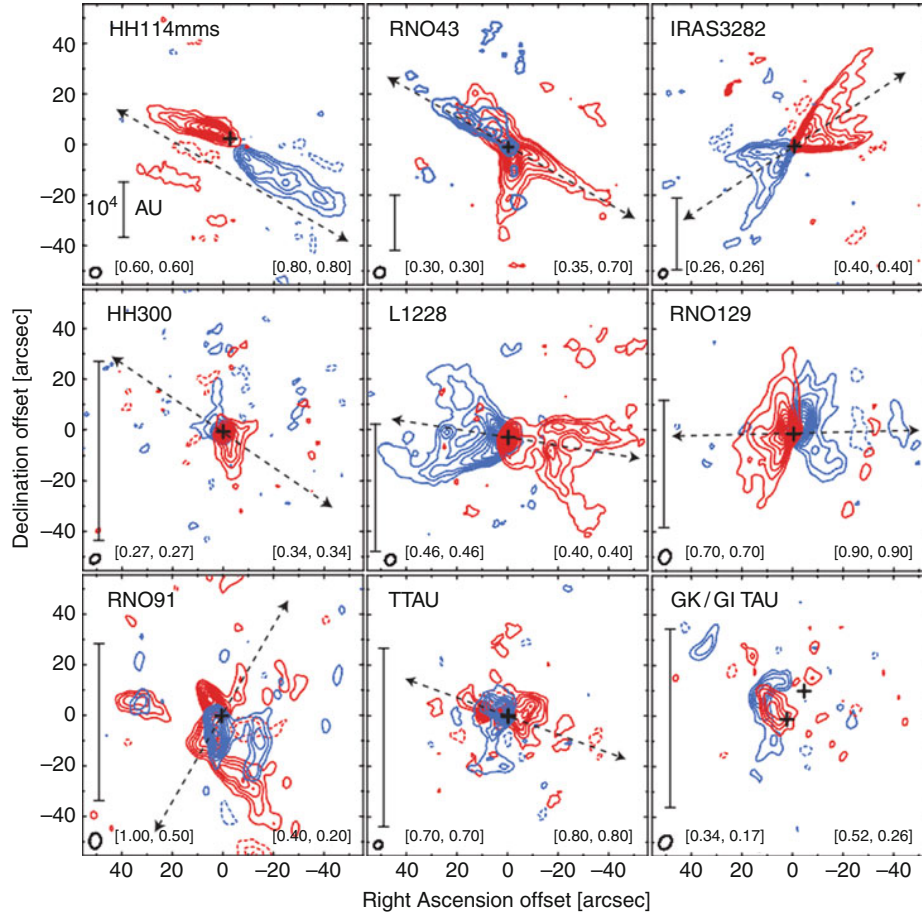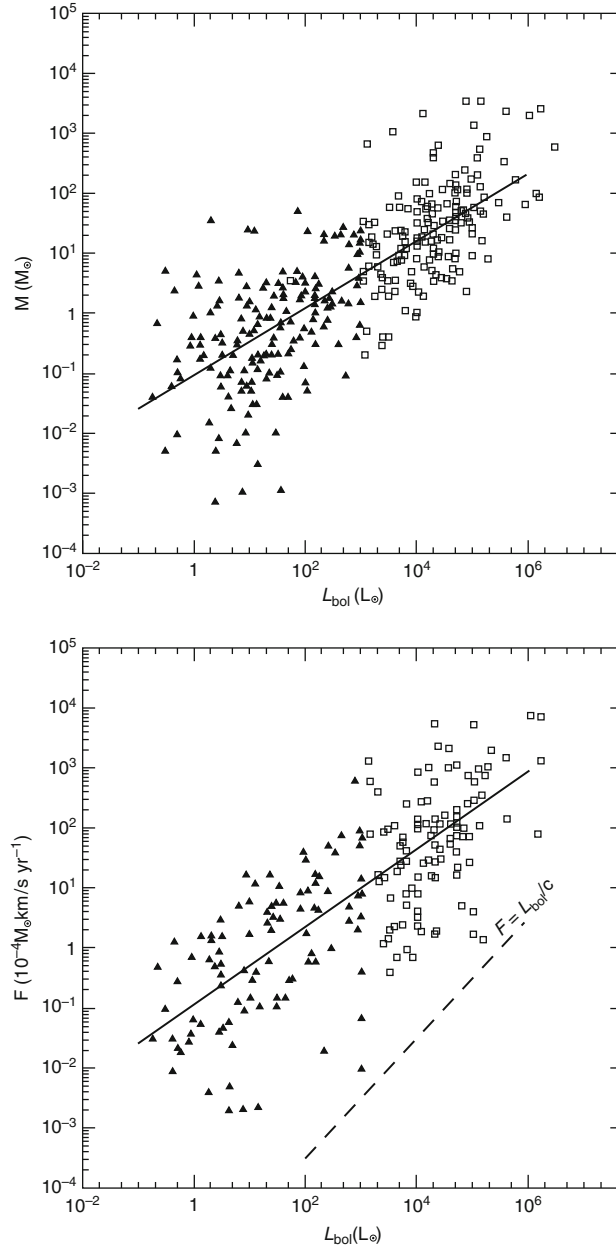
⬛ Fig. 6-18

Molecular outflows from Class 0 (*top*), I (*middle*), and II (*bottom*) sources after Arce and Sargent (2006)

to early B protostars suggesting a common accretion/outflow mechanism over a wide range of masses.

YSOs' outflows transfer momentum and entrain material from their surrounding molecular core/cloud by means of shock waves that propagate into the medium. Typical velocities are about few hundred km s^{-1} and produce prominent shock-excited nebulosities known as Herbig–Haro objects (or HHOs, see Reipurth 1999 for a catalog). HHOs are classified according to their electron temperature into two main groups: low excitation HHOs with $\log(T_e(K)) \leq 4$ and high excitation HHOs with $\log(T_e(K)) \geq 4.5$.

Low excitation HHOs are the result of mild oblique shocks mainly produced along the jet beam, as material from the surrounding cloud is entrained into the flow (see ❯ *Fig. 6-20*). HHOs' gas enters the shock front at several tens of km s^{-1} and most of the kinetic energy is damped into the excitation of the H_2 vibrational bands (in the infrared) as well as in radiation

◪ Fig. 6-19

Top: **CO outflow mass versus the bolometric luminosity (Lbol).** *Bottom:* **Outflow force *F* versus bolo-
metric luminosity (Lbol) of the associated infrared sources. Low mass YSOs and high mass YSOs
are represented with *filled triangles* and *open squares*, respectively. The fits given in the text are
represented in the figures (Wu et al. 2004)**
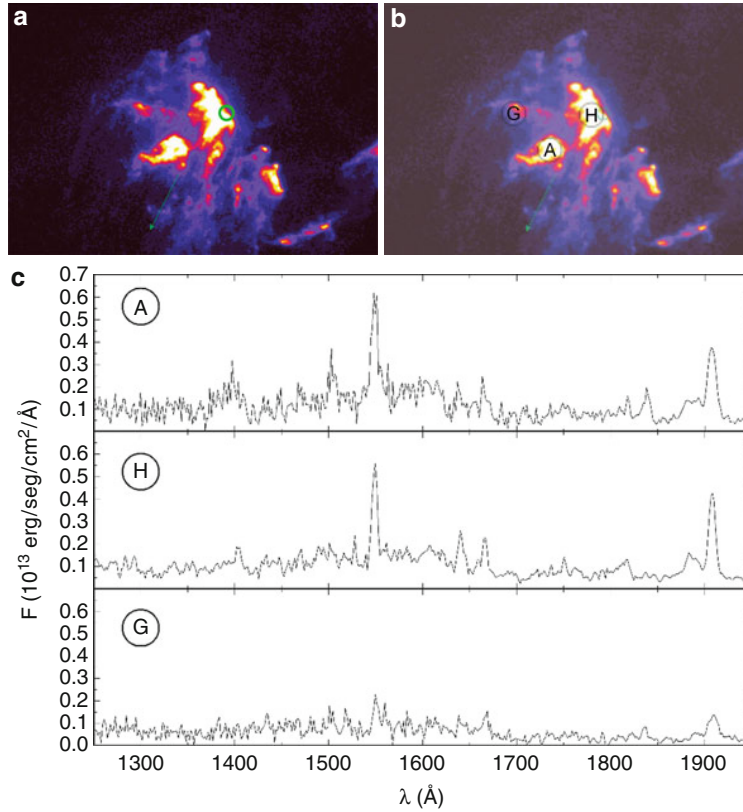
◼ Fig. 6-20
(a) The high excitation HHO: HH2. The location of the X-ray emission is marked with a *green circle*; the source of the flow is located in the direction traced by the arrow. The main knots in HH2H are marked in (b) and their UV spectrum (from the archive of the International Ultraviolet Explorer) is plotted in the bottom panel (c)

from the neutral/singly ionized species ([O I] and [S II] are among the most prominent optical tracers). The electron densities are $10–10^2$ cm^{-3} and the gas is only partially ionized with typical electron fractions of 0.1. Most of the molecular emission in the large-scale CO flows is also produced by gas entrained and accelerated in mild shocks. However, it is still unclear whether there is an additional, large scale, slow component made of rarified gas to the bipolar flow (Bachiller and Tafalla 1999).

High excitation HHOs mainly trace the bow shock or the working surface of the jet in high density environments. The kinetic energy of the jet is damped into heating producing very high temperatures that may reach $\sim 10^6$ K as observed in HH 2 (see ❷ *Fig. 6-21*). They may radiate from X-rays, in the most extreme cases, to the high excitation lines in the ultraviolet (i.e., He II o N V) and in the optical (i.e., [O III]). The electron densities are typically $10^3–10^4$ cm^{-3} and the gas is fully ionized. However, the predictions of strong radiative shock models are unable to reproduce fully the observations (Raymond et al. 1997), though this could be caused by the poor

Bynary
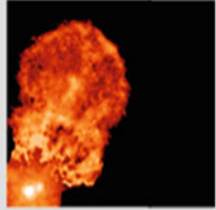
XZ Tau ($d = 140$ pc)   HH 111 ($d = 470$ pc)

Class 0

HH 49/50 ($d = 150$ pc)   HH 47 ($d = 450$ pc)   HH 211 ($d = 300$ pc)

Bow shock

HH 34 ($d = 470$ pc)

Irradiated jet

Jet in Triffid nebula ($d = 2{,}280$ pc)

◨ **Fig. 6-21**

Images of YSOs' jets. Jets from binary systems as XZ Tau or HH111 show wiggles and strong episodic ejections. Jets from class 0 sources are more deeply embedded in the cloud and interact strongly with the environment. Jets in clearer environments are highly collimated and produce bow shocks at the locations where the environmental conditions change. Finally irradiated jets are observed in several regions as Orion or the Triffid allowing a more reliable determination of the ionization fractions (Bally et al. 2006; Heathcote et al. 1996; Hester and Desch 2005; Krist et al. 1997; Reipurth et al. 1999; Tappe et al. 2008)

spatial resolution of the UV spectroscopic observations and the high clumpiness of HHOs. As an example, the UV-optical monitoring of HH 29 allowed to measure the inhomogeneity of the flow (Liseau et al. 1996) driving to a two-phase model of HHOs with a hot and dense component with $T = 10^5$ K and $n_e = 10^6$ cm^{-3} embedded into low excitation component at $T = 10^4$ K and $n_e = 10^3$ cm^{-3}. The estimated filling factor of the high excitation component was very small, barely ~0.1–1%.

Jets as large as 1–10 pc have been observed (i.e., the 10 pc flows detected in Orion; Reipurth et al. 1998). They provide the chance to study the midterm evolution of outflow (and accretion) on timescales of 5–50×10^3 year with a time resolution of ~10 years. As shown in ❯ *Fig. 6-21*, episodic ejections are common to all the YSOs' outflows. In fact, the collimated jets seem to result of the overlap of several shocked structures or knots. High activity and quiescent periods alternate during the flow evolution. Precession has been detected in a few sources (i.e., Cep E, Eisloffel et al. 1996) as well as bendings and misalignments suggesting variations in the outflow ejection direction. There are also indications of outflow rotation (Coffey et al. 2004). Evidence of magnetic fields have been reported for the outflow from T Tau S (Ray et al. 1997) and from several radio sources (Curiel et al. 1993).

4.1 First Steps to a Mechanism for Outflow Generation: Disk Winds

The high kinetic energy of the outflow requires an efficient launching mechanism that acts from the beginning of *Phase II* powered by accretion. The low effective gravity of the disk, the increasing centrifugal force as the star grows, and the disk ionization by the radiation from the accretion shocks creates the ideal environment to develop centrifugally driven outflows from the disk along the magnetic field lines permeating it.

Centrifugally driven outflows were first proposed in the context of Solar System research. The Sun is able to accelerate outflows from its slowly rotating atmosphere to ~400 km s^{-1} at the Earth orbit. These outflows depart through open holes in the magnetic configuration of the Sun. As the solar material is magnetized and, hence, firmly attached to the field lines, it leaves the Sun speeding up along the field lines like the water drops ejected from the nozzles of a rotating sprinkler. This magnetized outflow rotates rigidly with the Sun as far as the Alfvén radius, where the flow speed surpasses the Alfvén speed, i.e., the velocity at which information is transported in the magnetized flow (Weber and Davis 1967). Afterward, the flow evolves freely at this high speed. An important aspect of centrifugally driven winds is that they transport angular momentum away from the star. As the gas is forced to corotate with the star up to the Alfvén radius, r_A, it transports a specific angular momentum, $l_A = \Omega_* r_A^2$.

Blandford and Payne (1982) developed a version of centrifugally driven MHD winds for accretion disks. In their model, each ring of the disk is treated as a separate entity that rotates with Keplerian velocity. The disk is assumed to be permeated by an external field entering the disk in grazing incidence, as shown in the ❯ *Fig. 6-22*. Matter is loaded onto the lines and accelerated by the centrifugal lever arm. As the Solar MHD centrifugally driven winds, disk winds also carry a specific angular momentum *for each ring* given by $l_A = \kappa \Omega_{K,A} r_A^2$, where $\Omega_{K,A} r_A^2$ is the specific angular momentum at the Alfvén point and κ is a factor that depends on the precise geometry of the solution and ranges between 14 and 19 for simple self-similar solutions. Notice that the lever arm for angular momentum removal by MHD centrifugally driven winds is r_A, significantly larger than the level arm for viscous dissipation within the α-prescription,
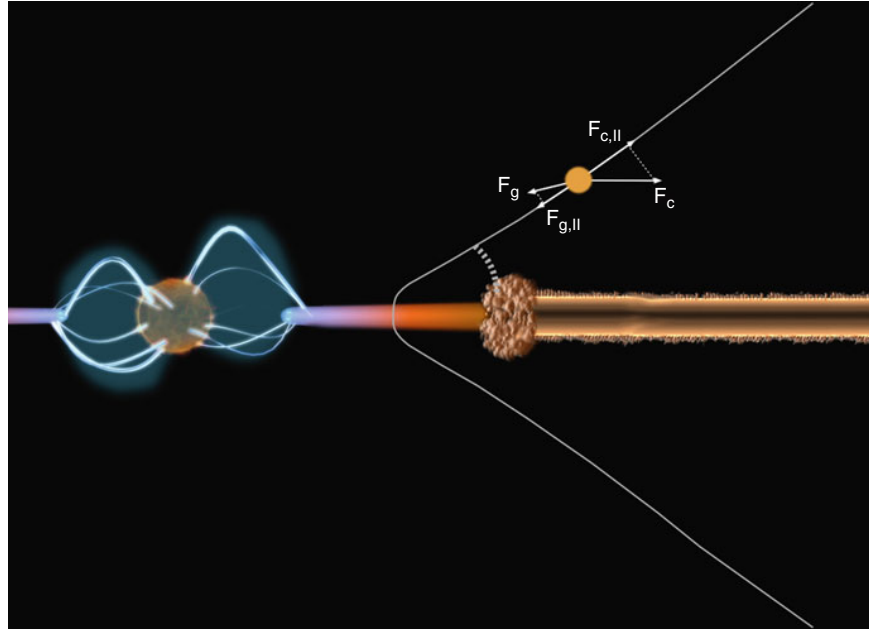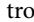
◩ Fig. 6-22
Sketch of the inner structure of low mass YSOs. The *inner disk* cavity filled in with hot gas is constrained between the stellar magnetosphere and the puffed up dusty rim that marks the separation between the heavily irradiated disk and the cool dusty disk. Disk winds depart along field lines that enter the disk in grazing angles acting like ramp speeds. If the centrifugal force projected along the field line is larger than the gravitational force, matter leaves the disk along the field lines and it is accelerated as far as the Alfvén radius

just αH. As a result, disk winds are an efficient mean to transport angular momentum and build up rapidly transport in YSOs' disks.

Disk winds extend the nested rings set up of the α-prescription for YSOs' disks into a nested Russian-dolls scheme that includes the large-scale outflow as a set of plasma sheets anchored in each ring (see ◗ *Fig. 6-23*). The velocity of matter flowing along this plasma sheet is usually projected into the three cylindrical components: rotation around the disk axis, expansion away from the rotation axis, and collimated motion along the axis. These components and their manifestation into unresolved line profiles are shown also in the figure. The dominant kinematics at the base of the outflow is radial expansion that produces very broad double-peaked profiles, rotation is only dominant very close to the Alfvén point and produces narrower double-peaked profiles, and further up, the dominant velocity is motion along the disk axis with a velocity $\sim\Omega_{K,A} r_A$.

Ferreira and Pelletier (1993, 1995) attached for the first time disk winds to α accretion disks. An interesting outcome is that outflows can only be generated in a very narrow range of plasma

βs^{11} with $2.84 < \beta < 3.12$ that only marginally intersect with the range where the MRI works; MRI ceases for $\beta > 3$.

The temperature of the outflow is regulated by three processes: (1) the rapid adiabatic radial expansion at the base, (2) heating by ambipolar diffusion, and (3) photoionization by the star. Ambipolar diffusion heating depends on the electron fraction of the wind. The higher the electron fraction, the smaller the heating. In YSOs' outflows, this results in an equilibrium temperature of about 10,000 K similar to that observed in the optical jets (Garcia et al. 2001; Safier 1993). However, if wind photoionization by the stellar X-ray photons is taken into account, the base of wind can reach temperatures of few thousand Kelvins (Ferro-Fontán and Gómez de Castro 2003). As shown in the ❯ *Fig. 6-24*, disk winds shield effectively the disk surface, protecting it from the high-energy X-ray photons from the star. In fact, they act as a protective layer that transforms the hard energy from the star into a milder (1,000–3,000 K) radiation field before it can reach the disk surface providing a wide spread source of heating of the disk atmosphere.

Disk winds are kept collimated by the pinching stress derived from the Lorentz force $\vec{J} \times \vec{B}$, where $\vec{J}$ is the current driven by the flow, mainly along the disk axis, and $\vec{B}$ is the magnetic field in the flow, mainly toroidal around the disk axis. This is a rich source of possible plasma large-scale instabilities, especially as flows depart from several radii in the disk. Pelletier and Pudritz (1992) showed that if the magnetic flux in the disk goes like $r^{-1/2}$, disk winds are stable since the same current is carried at all radii.[12] Typically the mass-loss rates estimated from disk winds modeling are about 10% of the accretion rate, in good agreement with the observational estimates.

YSOs' observations show that jets are not smooth laminar flows; instead, they show variable structures and knots. Some attempts were made in the past to reproduce this behavior through disk winds. Gómez de Castro and Pudritz (1993) showed that the unresolved forbidden line emission from jets could be produced by shocks at the magnetic refocusing points of disk winds. Garcia et al. (2001) and Ferreira and Casse (2004) attempted to reproduce the large-scale properties of jets by warm disk winds. In general, the coexistence of flows at different velocities from different disk radii, the interaction with the environment, and the pinching stresses are a rich source of oblique shocks and nonlinear interactions, especially amenable to numerical simulations, that can reproduce a large wealth of the observed phenomenology (see Pudritz et al. 2007 for a recent review in the field).

However, the observations clearly show that YSOs' bipolar outflows have a strong episodic component. The recognition that the interaction between the magnetosphere of a TTS and the disk would generate in a natural manner episodic ejections drove to the current paradigm for YSOs' outflow generation.

4.2 The Star–Disk Interface: The Jet Engine

Monitorings to derive the rotation rates of YSOs during *Phase III* revealed the existence of hot spots at temperatures of about 10^4 K on the surface of some TTSs (Bouvier 1990). This was further confirmed by UV monitorings (see Gómez de Castro 1998 for a review) raising the temperature of the spots to some $40,000$ K upon the detection of the flux modulation in the CIV line. In 1991, Koenigl showed that hot spots would be naturally produced if the accretion

---

[11]The β of plasma measures the rate between the thermal and the magnetic pressure, or, $\beta = (n k_B T)/(B^2/8\pi)$.
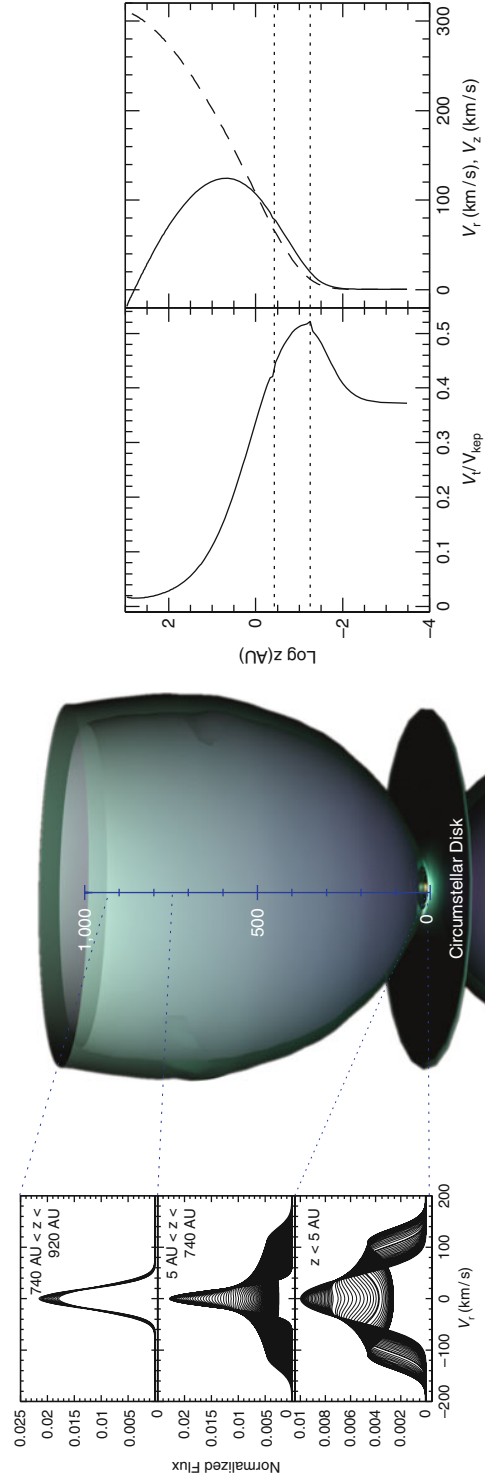[12]The self-similar solution corresponds to a scaling of the magnetic flux as $\propto r^{3/4}$.

■ **Fig. 6-23**

The basic kinematics of MHD centrifugal winds is outlined from the simple semiempirical model of centrifugally driven MHD winds with thermal pressure of Gómez de Castro and Ferro-Fontán (2005). In the _central panel_, the nested plasma sheets are represented. To the _right_, the properties of the velocity field in the flow are described; the variation of the toroidal (V_t), radial (V_r) and axial (V_z) components with the height above the disk midplane are represented. The toroidal component is scaled with respect to the Keplerian velocity of the disk at the radius from which the wind is ejected. V_r and V_z are plotted in the rightmost inset with _solid and dashed lines_, respectively. The location of the Alfvén points is marked with _horizontal dashed lines_. In the _left panel_, line profiles generated by rings of gas in the flow, at different heights along the z-axis (the disk axis) are represented for an observed at $i = 90°$ (disk seen edge-on)
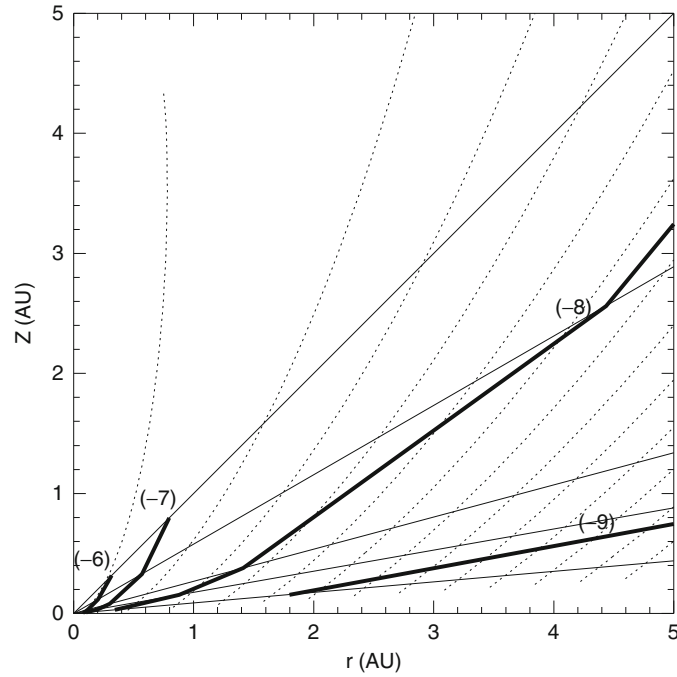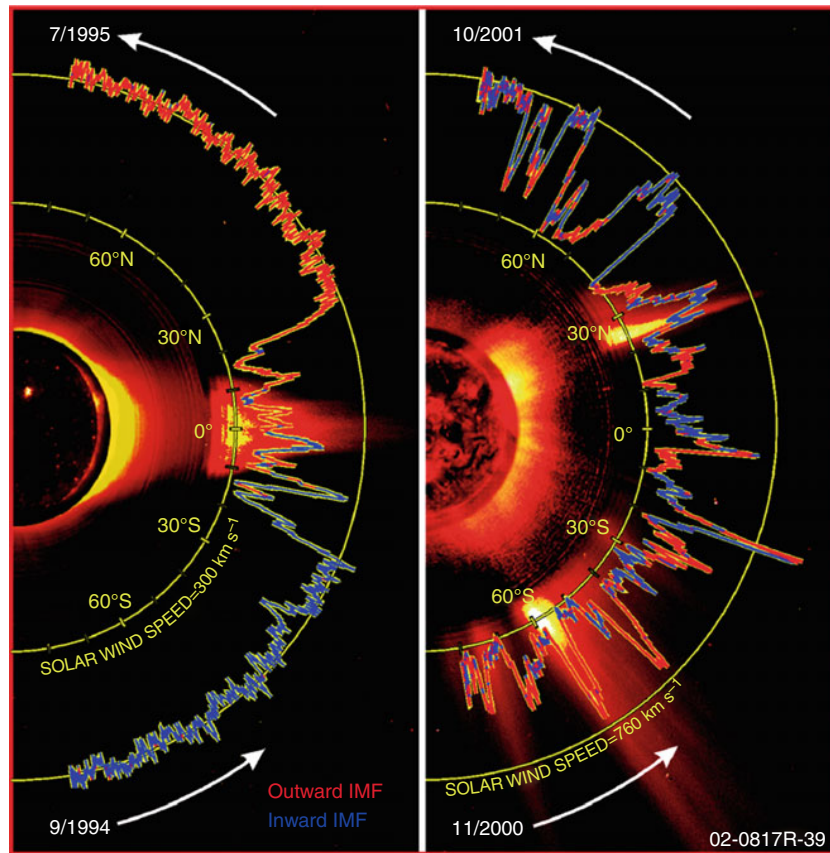
◙ Fig. 6-24

Surfaces where the temperature reaches 4,000 K due to photoionization of the disk wind by the stellar X-ray field. The *thick solid lines* represent the isotemperature surfaces for accretion rates of 10^{-6}, 10^{-7}, 10^{-8} and 10^{-9} solar masses per year as marked by the numbers in brackets. The *thin dashed lines* represent the flow lines of matter in the jet. The *thin solid lines* mark the direction of colatitude ϑ = 45°, 60°, 75°, 80° and 85° (from Ferro-Fontán and Gómez de Castro 2003)

flow from the disk is channeled by the stellar magnetic field onto the star. The stellar field is assumed to be anchored in the inner part of the disk creating a sheared layer between the rigid body rotation of the star and the Keplerian rotation of the disk. This interaction has a profound influence on the star and the accretion flow but also acts as a dynamo that transforms part of the angular momentum excess in the inner disk into magnetic field amplification that self-regulates through quiescent periods of field building up and eruptions when the energy excess is released.

The basic physics is rather simple: the stellar magnetic field acts like the magneto in the dynamo that is able to drive currents by means of the Lorentz force into the material falling under the action of gravity. There are, however, a great number of uncertainties in the way the system self-regulates and also on the dependence of the engine details on the initial conditions such as the effective gravity of the star, the role of stellar radiation and magnetic field on the engine performance, and the role of the ionizing radiation produced by the engine on the evolution of the mass storage, the disk.

Going forwards on time: the Sun, itself, provides important clues to understand the physics of this gravito-magnetic engine and its evolution. At the base of the Sun convective layer, the tachocline marks the location of the shear layer between the rigid body rotation of the radiative core and the differentially rotating convective envelope. The radial gradient of the angular

velocity changes sign becoming negative for latitudes $>35°$ and positive above this latitude. This latitude marks the limit of the two latitude belts where the overwhelming majority of sunspots occur. There are also some indications of the meridional flow moving equatorward below this latitude and poleward above it (see Miesch 2005). The Solar wind is (magnetic) latitude dependent during solar minimum; above $\sim35°$ is fast $(1,000\,\mathrm{km\,s^{-1}})$ and thin, below $\sim35°$ is slow $(300\,\mathrm{km\,s^{-1}})$ and dense (see ❷ *Fig. 6-25* from Ulysses data). The current paradigm for how solar dynamo operates includes: (1) field amplification in a turbulent downflow (α effect) that is pumped downward by convection and accumulated in the overshoot region and the tachocline;

◪ **Fig. 6-25**
Solar wind observations collected by the Ulysses spacecraft during two separate polar orbits of the Sun, 6 years apart, at nearly opposite times in the solar cycle. Near solar minimum (*left*) activity is focused at low altitudes, high-speed solar wind prevails, and magnetic fields are dipolar. Near solar maximum (*right*), the solar winds are slower and more chaotic, with fluctuating magnetic fields (From NASA Solar Probe Web (solarprobe.gsfc.nasa.gov), courtesy of Southwest Research Institute and the Ulysses/SWOOPS team)

(2) field amplification and organization into toroidal flux tubes and sheets by differential rotation in the tachocline; (3) magnetic instabilities (buoyancy) drives the field to the surface, and (4) the Coriolis force acting on the rising structures to produce a latitude-dependent emergence of bipolar magnetic structures.

Going backward in time, during star formation, there is an "external tachocline" or differentially rotating region attached to the stellar surface (the outer part of the convective layer). This *external tachocline* connects the star with the accretion disk which rotates significantly more slowly than the stellar surface; rotation periods of TTSs are about 7–8 days ($\Omega_* = 0.8-0.9$ day^{-1}) while the Keplerian frequency is:

$$\Omega_k = 0.6 \text{ day}^{-1} \left(\frac{M}{M_\odot} \right)^{1/2} \left(\frac{r}{3R_\odot} \right)^{-3/2}$$

Keplerian disk corotation radius is at

$$r_{\text{corot}} = 17.5 \, R_\odot \left(\frac{M}{M_\odot} \right)^{1/3} \left(\frac{P}{8 \text{ days}} \right)^{2/3}$$
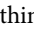
To avoid this large shear, the magnetosphere grows to balance the toroidal component of the flux with the angular momentum of the infalling matter (Ghosh and Lamb 1979) thus,

$$\frac{B_p B_t}{4\pi} 4\pi r^2 \Delta r \simeq \dot{M}_a r V_k$$

where B_p and B_t are the poloidal and toroidal components of the field, respectively, r is the magnetosphere radius, Δr is the thickness of the shear layer, $\dot{M}_a$ is the accretion rate, and V_k is the Keplerian velocity at the magnetospheric radius. For typical T Tauri star parameters:

$$r_{\text{mag}} = 4.4 R_\odot \gamma^{2/7} \left(\frac{B_*}{1kG} \right)^{4/7} \left(\frac{\dot{M}}{10^{-8} M_\odot \text{year}^{-1}} \right)^{-2/7} \left(\frac{M_*}{M_\odot} \right)^{-1/7}$$

where $\gamma^{2/7}$ is a factor about unity ($\gamma = (B_t/B_p)(\Delta r/r)$, see Lamb 1989). Notice that the main uncertainties in the physics, namely, the ratio between the toroidal and the poloidal components and the relative thickness of the *external tachocline*, are enclosed in this factor.

As in the Solar interior, the shear region is fed by turbulent, magnetized material, though in YSOs, this comes from the accretion disk. Shear amplifies the field producing a strong toroidal component and a dynamo sets in an extended stellar magnetosphere. This toroidal field and the associated magnetic pressure push the field lines outward from the disk rotation axis, inflating and opening them in a *butterfly-alike pattern* reminiscent of the helmet streamers in the solar corona. As a result, a current layer is produced between the region dominated by a hot and thin stellar wind and the area where the disk wind is ejected from as displayed in ❯ *Fig. 6-26*. Magnetic field dissipation in the current layer produces high-energy radiation and particles. The magnetic link between the star and the disk is broken and reestablished continuously by magnetic reconnection as shown in the figure. The opening angle of the current layer, as well as its extent, depends on the stellar and disk fields, the accretion rate, and the ratio between the inner disk radius and the stellar rotation frequencies. Hot, pressure-driven outflows are produced from the region closer to the rotation axis while centrifugally driven flows are produced by the disk; plasmoids are ejected from the current layer generating a third outflowing episodic component.

Disk–star interaction has been investigated since the early concepts of X-winds (see Shu et al. 2000 for a review) to the numerical simulations by Goodson et al. (1997) and the last
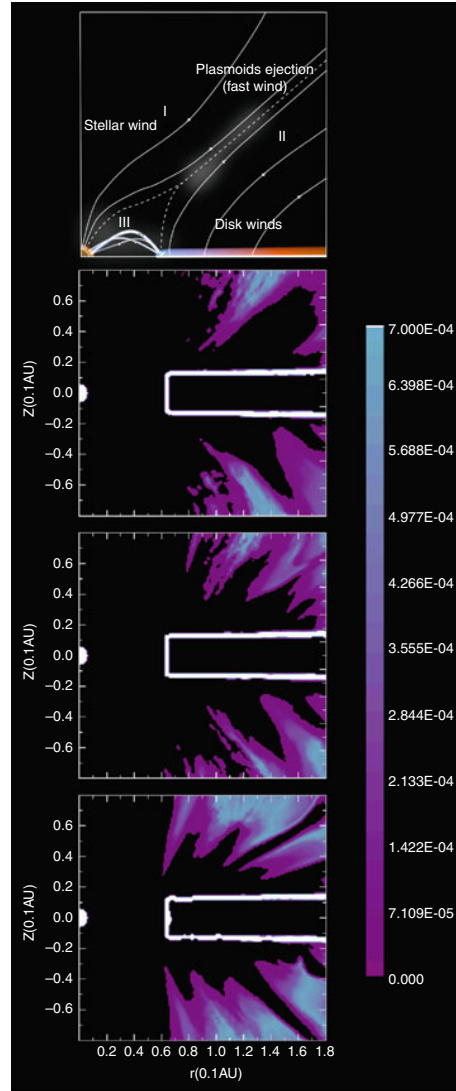
◪ **Fig. 6-26**

The interaction between the stellar magnetic field and the disk twists the stellar field lines due to the differential rotation. The toroidal magnetic field generated out of the poloidal flux and the associated pressure tends to push the field lines outward, inflating them, and eventually braking the magnetic link between the star and the disk (boundary between Regions I and II). Three basic regions can be defined: Region I dominated by the stellar wind, Region II dominated by the disk wind, and Region III dominated by stellar magnetospheric phenomena. The *dashed line* traces the boundaries between these three regions. The *continuous lines* indicate the topology of the field and the shadowed areas represent regions where magnetic reconnection events are likely to occur, producing high-energy radiation and particles. UV radiation released by the plasma heated in this interaction going from quiescence (*top*) to outburst (*bottom*) after Gómez de Castro and von Rekowsky (2011)

results (i.e., von Rekowski and Brandenburg 2006). They show that the fundamental mechanism for disk winds formation is robust; numerical simulations with different parameters (disk/star fields) and initial conditions produce disk winds. Stellar winds are much more sensitive to the physical conditions and, especially, to the stellar field. The characteristics of the accretion flow and the winds (dominant driver, temperature, terminal velocity, density, variability) depend on the physical properties of the system such as the degree of magnetization of the disk, the characteristics of the disk dynamo, and the stellar field. During *Phase III*, the bulk of the energy losses of the engine are radiated at UV and X-ray wavelengths as in the Sun atmosphere (though a large fraction of the high energy radiation is reprocessed to longer wavelengths in the YSOs environment at early stages).

This paradigm is based (and inspired) in the Sun thus, naturally, applies to low mass YSOs with well-defined stellar fields; it is yet unclear how to adapt it to HAeBe stars and, in general, to massive YSOs. However, Ae Herbig stars have a rich UV emission-line spectrum consistent with the presence of a chromosphere above the photosphere (Brown et al. 1996; Deleuil et al. 2005). Also, overionized species (transition region or corona-like) are observed. Magnetic field dissipation seems the most likely source for the radiative losses in the chromosphere/wind that represent 4–8% of the stellar bolometric luminosity according to Bouret and Catala (1998), although accretion flows may be a non-negligible energy source (Blondel et al. 1993). Marginal detection of magnetic fields has been reported for HD 104237 (Donati et al. 1997).

Further evidence to the presence of magnetic fields in the Ae Herbig stars atmospheres comes from the detection of azimuthal structures in the wind of AB Aur (Praderie et al. 1986). They are best interpreted resourcing, again, to the Solar wind and assuming that the very hot clumps are produced in the shocks between a "high" velocity component made by streamers of magnetically confined gas and a dense and "slow" outflow driven by radiation. In this sense, the hot clumps would be tracing a PMS analogue to the Solar Corotating Interaction Regions (CIRs). Evidence of such a class of structures has also been found in a Class III TTS: AB Dor (Gómez de Castro 2009).

Though observations suggest that fields are present in Ae Herbig stars, at least, during the first $\sim 5 \times 10^6$ years of their PMS evolution, the ultimate source of the field remains unidentified. Turbulence and rotation could set up a dynamo in the outer stellar layers. Turbulence can be generated by stellar pulsation; radial and nonradial modes have been detected with periods from some tens of minutes to hours (see Catala 2003 for a review). Also, the rotational braking produced by the strong stellar wind could induce turbulent motions below the stellar surface, forcing magnetic fields into the outer stellar layers (Lignieres et al. 1996).

Accretion is not expected to be the only driver of the outflow in these luminous sources. Radiatively driven winds are also able to produce collimated outflows provided there is a magnetic field (Rotstein and Gimenez de Castro 1996).

4.3 The Stellar Magnetosphere

The stellar magnetosphere is the key structure in the engine. Magnetic fields of few kG have been detected in the surface of the TTSs (Guenther et al. 1999; Johns-Krull et al. 1999). The surface field is not bipolar but has a rather complex structure as in the Sun (Johns-Krull et al. 2004). Higher order multipolar components fall off more rapidly with radius than the dipolar field hypothesized for the engine, making extremely difficult to track the path followed by matter
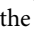
from the inner disk border to the stellar surface. In addition, the magnetosphere has its own dynamics and forcing due to the interaction with the disk.

4.3.1 Accretion Shocks and Funnels

The accretion flow has a clearly identifiable episodic component produced by the capture of material from the inner border of the disk into magnetic loops or funnels that drive it into the stellar surface. The kinetic energy of the infalling material is released into heating at the impact point. As matter infall occurs along the field lines, all the gravitational energy is damped into heating and the gas may reach temperatures as high as $\sim 10^6$ K. The dominant output radiation is produced by the photoionized preshock infalling gas radiating mainly in the UV range; the shock front itself radiates in soft X-rays (Gullbring et al. 2000; Lamzin 1998). As the density of the infalling gas column is high ($n_e \simeq 10^9 - 10^{12}$ cm^{-3}) the thickness of the radiating column is expected to be negligible compared with the stellar radius; thus, accretion shocks are observed as *hot spots* on the stellar surface. As such, they are expected to produce a rotationally modulated signal at high energies that is especially strong at the shortest wavelengths (see Petrov et al. 2001 or Bouvier et al. 2003 for optical monitorings and Gómez de Castro 1998 for UV monitorings). A soft X-ray excess is reported for actively accreting TTSs that would trace the location of the $\sim 10^6$ K shock front (Guedel and Telleschi 2007). The presence of infalling gas cloudlets is detected in the redwing of the line profiles of many species tracing warm plasma (H$_\alpha$, Mg II, Ca II, etc.); however, there are very few monitorings tracking the motion of gas parcels as they fall onto the star, and when this is done, a correlation is found between accretion and outflow (RU Lup: Stempels and Piskunov 2002; RW Aur: Gómez de Castro and Verdugo 2003 and AA Tau: Bouvier et al. 2007). Four interesting features have been derived from the observations:
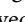
1. The interaction between the magnetosphere and the disk may drive to the formation of warps in the inner disk as reported for AA Tau (Bouvier et al. 2003).
2. The end points of the accretion funnels cover just a few percent of the stellar surface (Bouvier et al. 2007).
3. Accretion flows may switch on or switch off on timescales of a few years without large variations in the overall properties of the star or the disk as observed in RY Tau (Gómez de Castro 2009).
4. The hot plasma ($4 < \log T_e(K) < 5$) tracers registering the accretion shocks, as for instance the He I 10830 (Fischer et al. 2008) or the UV lines, indicate that there is an extended magnetospheric component in addition to the accretion shock emission. Only $\sim 50\%$ of the UV continuum excess is rotationally modulated (Gómez de Castro 2009).

4.3.2 General Magnetospheric Properties

Unfortunately, the characteristics of the TTSs extended magnetospheres are still escaping the diagnosis (see Hartmann 2009). Further to some qualitative properties as that outlined in the sketch in ❷ *Fig. 6-26*, little is known about TTSs magnetospheres apart from having a density of about 10^9–10^{10} cm^{-3} and an electron temperature between some few thousand Kelvin and 100,000 K. The line widths of typical atmospheric/magnetospheric tracers are about

200–300 km s^{-1} that exceed by far what was expected from thermal broadening or from rotational broadening even if the lines are assumed to be formed in a corotating magnetosphere that extends to some 4–5 stellar radii.

The source of these large broadenings remains evasive since the very beginning of the studies of TTSs atmospheres. In the 1980s, line broadening was modeled with macro turbulence fields in a very massive outflow (Calvet et al. 1985). Later on, magnetospheric accretion was proposed to explain the large broadening of the TTSs Hα lines (Muzerolle et al. 1998). Infall adds an extra radial velocity component to the rotation of the radiating gas that has an effect in the line profiles somewhat similar to that shown in ❯ Fig. 6-23 for the outflow. As free-fall velocities are comparable to the broadening[13], the observe profile widths can be reproduced without difficulty tuning the curvature of the plasma trajectory from the inner disk into the stellar surface. However, there must be a dependence on the inclination that has not been clearly identified on the spectrally resolved observations of magnetospheres. As of today, it is still unclear whether the broadening is produced by unresolved macroscopic flows or by magnetic waves propagating on the magnetospheric field. In general, the broadening of magnetospheric tracers does not vary significantly pointing out that the average motions are rather stable. The combined effect of funnel flows and inclined magnetic rotators as simulated by Romanova et al. (2004) is the current baseline for the numerical simulation of TTSs magnetospheres.

Magnetospheres are assumed to produce the truncation of the inner disk producing the observed holes in the molecular gas distribution (see ❯ Sect. 3). As the disk is not unlocked from the magnetosphere, it is expected to be subjected to the propagation of the Alfvén waves, shear waves, and global alfvén oscillations driven from the interface. The inner rim of the disk is expected to be hot with temperatures of about 10^4 K. Evidence for such a structure has been found only in RW Aur (Gómez de Castro and Verdugo 2003).

5 Some Final Thoughts and Conclusions

Star, disk, and outflow are the three components of a basic gravitational engine. The star grows out of the accretion flow and it is the most stable element of the system. After reaching a critical mass, the spheroid reaches hydrostatic equilibrium and any collision or dramatic event leading to the partial or total disruption of the disk will just reduce its final mass making the star formation process just more inefficient. Thus stars and disk ages do not always match.

Disks have a profound effect on stellar evolution since the magnetic interaction between the star and the disk controls the evolution of angular momentum during star formation. As soon as the star–disk locking is released, YSOs follow the hydrostatic contraction to the ZAMS speeding up as the radius decreases and the mass distribution in the star gets more centrally peaked. As a result, the Class III TTSs rotate faster than the Class II (see Choi and Herbst 1996) and a broad distribution of rotation periods is expected among stars of the same mass in the same molecular cloud depending on the timing of the disk unlocking.

There is, however, a link between the age of young associations as a whole and the rotation spread of their member stars. As an example, the spread of velocities observed in α Per (a 50 Myr old stellar association) is 150 km s^{-1} for G-type stars (0.8–1.0 M$_\odot$) (Prosser 1992). However no

---

[13]Typical free-fall velocities are:$v_{ff} \simeq 315 \, \text{kms}^{-1} \left(\frac{M_*}{M_\odot} \right)^{1/2} \left(\frac{R_*}{R_\odot} \right)^{-1/2}$.
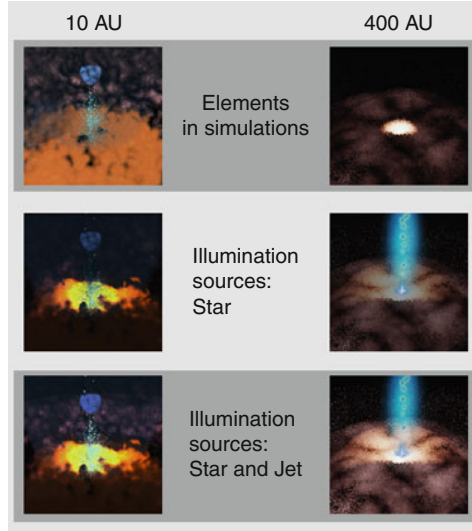
■ Fig. 6-27

Simulation of the effect of the outflow and the inflated magnetic structure on the disk irradiation.
***Top*, YSOs' components; *middle*, only stellar illumination is switched on; *bottom*, full illumination, including the jet. The density in the disk is simulated by seven nested surfaces that act as boundaries to volumes filled with 10^6 particles each, up to a grand total of 7×10^6 particles in the disk. The surfaces have been selected from the final density distribution in the gravitational collapse simulations of ❯ *Fig. 6-9* (bottom panel of ❯ *Fig. 6-9a*). The density levels correspond to $\Delta \log \rho = 0.6$. The optical performance of the particles is characterized by an albedo of $57 \pm 2\%$**

spread is observed among G-type stars in the older Pleiades association (100 Myr old) while K dwarfs still display a broad dispersion in rotation velocities (Mayor and Mermilliod 1991) that is lost in the even older Hyades association (Stauffer et al. 1997). This indicates that once the disk locking is lost, a Solar-like wind develops braking the stellar rotation. As the total angular momentum of the system ought to be conserved, the angular velocity of the star decreases at a rate of roughly $l_A \dot{M}_w$, where $\dot{M}_w$ is the wind mass-loss rate (for the Sun currently is $\sim (2-3) \times 10^{-14} M_\odot \text{year}^{-1}$). As the lever arm (the Alfvén radius) is larger for faster rotators, they brake more efficiently than the slower ones reaching an equilibrium configuration in some tens of Myrs.

Stars and the accretion engine control the irradiation of the disk and its lifetime. The base of the outflow and the reconnection at the star–disk interface is an abundant source of hard UV radiation that has a profound impact into disk evolution and chemistry. The geometrical location of the illuminating source is relevant to determine the flux that reaches the disk surface. As shown in ❯ *Fig. 6-27*, the effect of the outflow and the inflated magnetic structure on the disk irradiation ought to be taken into account. High latitude illumination facilitates energy absorption by the disk. The simulation shown in the figure is made with ray-tracing algorithms. The YSO's environment is simulated assuming a density law as in Yorke and Bodenheimer (1999) to model the protostellar disk. The disk is irradiated by three sources (star, extended magnetosphere, and jet). The luminosity of the star is assumed to be $L_\odot$, the luminosity of the extended magnetosphere to be 10% of this value, and the luminosity of the jet $0.01 L_\odot$. The system was scaled to

■ Fig. 6-28

Molecular gas in the Gould's Belt from Dame (2001)
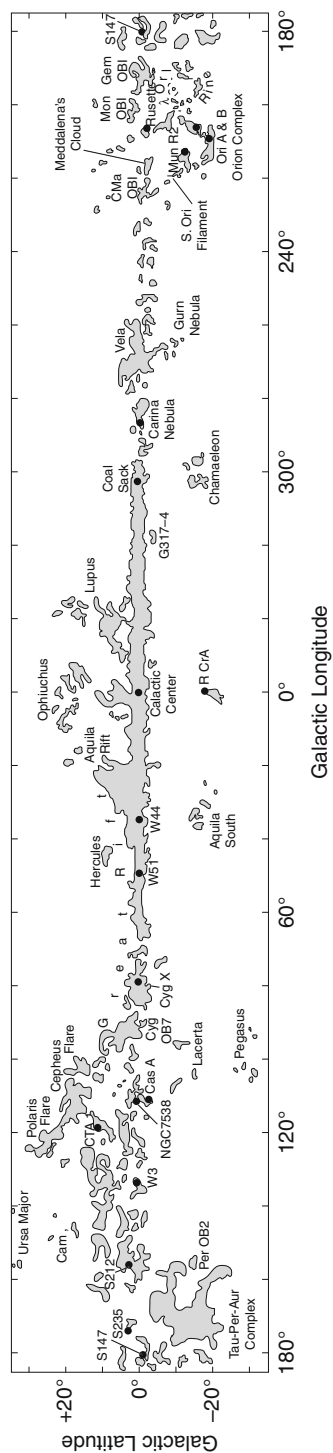
represent a solar mass star. The effect of the jet in the disk irradiation can be drawn by comparing the two lower panels where the jet contribution to the disk illumination is switched on/off. Unfortunately, the current uncertainties on the inner structure of the engine and the properties of the magnetosphere make this kind of studies extremely model dependent.

In the coming years, the understanding of YSOs and protostellar disks evolution will suffer a major revolution due to the impact of the new facilities, now under development, for (1) high spatial resolution (1 AU scales) mapping of the molecular emission of protostellar disks and (2) dedicated monitorings of the YSOs high-energy output at UV wavelengths to map the magnetospheric structure and the inner engine.

Acknowledgments

Appendix A: The Gould's Belt

The Gould's Belt is the local super association of star formation and has characteristics similar to a starburst. Molecular gas, early B to A stars, star forming regions, and young associations as the Pleiades or the Hyades form part of the belt. The extent of the belt is about 800 pc and the Sun is located at about 160 pc of its innermost border (see Poeppel 1997 for a review). Around the position of the Sun, there is an inner belt of radius 140 pc where the main star forming regions are located: Taurus-Aurigae, Ophiuchus, Lupus, Chamaleon, Sco-Cen, and Serpens (see ❯ *Fig. 6-28*). There are not very massive O-type stars in the belt. The origin of the Gould's Belt is unknown. The constituents of the belt share a common kinematics and are located in a plane inclined with respect to the galactic plane by 16°. Three main formation scenarios have been proposed to explain its characteristics: a supernovae explosion (Perrot and Grenier 2003), the impact of a high velocity cloud from the halo (Comerón and Torra 1994), and the formation of a corrugated galactic disk due to the onset of the Parker instability (Gómez de Castro and Pudritz 1992).

References

Abraham, P., Kospal, A., Csizmadia, Sz., et al. 2004, A&A, 428, 89

Adams, F. C., Lada, Ch. J., & Shu, F. H. 1987, ApJ, 312, 788

Adams, F. C., Ruden, S. P., & Shu, F. H. 1989, ApJ, 347, 959

Alexander, D. R., & Ferguson, J. W. 1994, ApJ, 437, 879

Alexander, R. D., Clarke, C. J., & Pringle, J. E. 2006, MNRAS, 369, 1, 229

Andersen, J. 1991, Astron Astrophys Rev, 3, 91

Andersen, J., Lindgren, H., Hazen, M. L. et al. 1989, A&A, 219, 142

Andre, Ph., Martin-Pintado, J., Despois, D. et al. 1990, A&A, 236, 80

Andre, P., Ward-Thompson, D., & Barsony, M. 2000, Protostars and Planets IV (Tucson: University of Arizona Press), 59

Arce, H. G., & Sargent, A. I. 2006, ApJ, 646, 1070

Armitage, P. J., Livio, M., & Pringle, J. E. 2001, MNRAS, 324, 705

Arons, J., & Max, C. E. 1975, Astrophys J Lett, 196, L77

Bachiller, R., & Tafalla, M. 1999, The Origin of Stars and Planetary Systems (Dordrecht: Kluwer), 227

Bachiller, R., Pérez Gutiérrez, M., Kumar, M. S. N. et al. 2001, A&A, 372, 899

Balbus, S. A., & Hawley, J. F. 1991, ApJ, 376, 214

Balbus, S. A., & Papaloizou, J. C. B. 1999, ApJ, 521, 650

Bally, J., O'Dell, C. R., & McCaughrean, M. J. 2000, AJ, 119, 2932

Bally, J., Walawender, J., Luhman, K. L. et al. 2006, AJ, 132, 1930

Beckwith, S. V. W., Sargent, A. I., Chini, R. S. et al. 1990, Astronom J, 99, 924

Behrend, R., & Maeder, A. 2001, A&A, 373, 190

Bell, K. R., & Lin, D. N. C. 1994, ApJ, 427, 987

Bell, K. R., Lin, D. N. C., Hartmann, L. W. et al. 1995, ApJ, 444, 376

Bertoldi, F. 1989, ApJ, 346, 735

Blandford, R. D., & Payne, D. G. 1982, MNRAS, 199, 883

Blondel, P. F. C., Talavera, A., & Djie, T., 1993, A&A, 268, 624

Boehm-Vitense, E. 1958, Zeitschrift fur Astrophysik, 46, 108

Bonnor, W. B. 1957, MNRAS, 117, 104

Bouret, J. C., & Catala, C. 1998, A&A, 340, 163

Bouvier, J. 1990, *Astronomical Journal*, 99, 946

Bouvier, J., Grankin, K. N., Alencar, S. H. P. et al. 2003, A&A, 409, 169

Bouvier, J., Alencar, S. H. P., Boutelier, T. et al. 2007, A&A, 463, 1017

Braginskii, S. I. 1965, Rev Plasma Phys, 1, 205

Brown, A., Deeney, B. D., Ayres, T. R. et al. 1996, ApJS, 107, 263

Calvet, N., Basri, G., Imhoff, C. L., et al. 1985, ApJ, 293, 575

Canuto, V. M., & Mazzitelli, I. 1991, ApJ, 370, 295

Casey, B. W., Mathieu, R. D., & Vaz, L. P. R. 1998, Astronom J, 115, 1617

Catala, C. 2003, Magnetism and activity of the sun and stars. Proceedings of the Conference held 17–21 September, 2002 in Toulouse, France. EAS Publication Series, Vol. 9 (Les Ulis: EDP Sciences), 325

Caughlan, G. R., & Fowler, W. A. 1988, Atomic Data and Nuclear Data Tables, 40, 283

Cesaroni, R., Neri, R., Olmi, L. et al. 2005, A&A, 434, 1039

Cesaroni, R., Galli, D., Lodato, G. et al. 2007, Protostars and Planets V, Vol. 951 (Tucson: University of Arizona Press), 197

Chen, H., Myers, P. C., Ladd, E. F. et al. 1995, ApJ, 445, 377

Choi, P. I., & Herbst, W. 1996, Astronom J, 111, 283

Clampin, M., Krist, J. E., Ardila, R. D. et al. 2003, AJ, 126, 389

Coffey, D., Bacciotti, F., Woitas, J. et al. 2004, ApJ, 604, 758

Collins, J. A., Shull, J., & Giroux, M. L. 2009, ApJ, 705, 962

Comerón, F., & Torra, J., 1995, A&A, 423, 652

Comerón, F., & Torra, J., 1994, A&A, 241, 57

Covino, E., Frasca, A., & Alcal, J. M. 2004, A&A, 427, 637

Curiel, S., Rodriguez, L. F., Moran, J. M. et al. 1993, ApJ, 415, 191

D'Antona, F., & Mazzitelli, I. 1997, Memorie della Societa Astronomia Italiana, 68, 807

D'Alessio, P., Canto, J., Calvet, N. et al. 1998, ApJ, 500, 411

Dame, T. M. (2001), in Atoms, Ions and Molecules: New Results in Spectral Line Astrophysics, ASP Conf. Ser. (San Francisco: ASP), 16, 43

Deleuil, M., Bouret, J.-C., Catala, C. et al. 2005, A&A, 429, 247

Donati, J. F., Semel, M., Carter, B. D. et al. 1997, MNRAS, 291, 658

Draine, B. T. 1978, Astrophys J Suppl Series, 36, 595

Dunham, M. M., Evans, N. J., Terebey, S. et al. 2010, ApJ, 710, 470

Durisen, R. H., Boss, A. P., Mayer, L., et al. 2007, in Protostars and Planets V, eds. B. Reipurth, D. Jewitt, & K. Keil (Tucson: University of Arizona Press), 607

Dutrey, A., Guilloteau, S., & Simon, M. 2003, A&A, 402, 1003

Dutrey, A., Guilloteau, S., & Ho, P. 2007, Protostars and Planets V, Vol. 951 (Tucson: University of Arizona Press), 495

Edris, K. A., Fuller, G. A., Cohen, R. J. et al. 2005, A&A, 434, 213

Eisloffel, J., Smith, M. D., Davis, C. J. et al. 1996, Astronom J, 112, 2086

Evans, N. J., Dunham, M. M., Jorgensen, J. K. et al. 2009, Astrophys J Suppl Series, 181, 321

Ferreira, J., & Pelletier, G. 1993, A&A, 276, 625

Ferreira, J., & Pelletier, G. 1995, A&A, 295, 807

Ferreira, J., & Casse, F. 2004, Astrophys Space Sci, 292, 479

Ferro-Fontán, C., & Gómez de Castro, A. I. 2003, MNRAS, 342, 427

Fischer, W., Kwan, J., Edwards, S. et al. 2008, ApJ, 687, 1117

Font, A. S., McCarthy, I. G., Johnstone, D. et al. 2004, ApJ, 607, 890

Froebrich, D. 2005, Astrophys J Suppl Series, 156, 169

Furlan, E., Hartmann, L., Calvet, N. et al. 2006, Astrophys J Suppl Series, 165, 568

Gail, H. P. 2004, A&A, 413, 571

Gammie, Ch. F. 1996, ApJ, 457, 355

Gammie, Ch. F. 2001, ApJ, 553, 174

Garcia, P. J. V., Ferreira, J., Cabrit, S. et al. 2001, A&A, 377, 589

Garrod, R. T., & Herbst, E. 2006, A&A, 457, 927

Garrod, R. T., Vasyunin, A. I., Semenov, D. A. et al. 2009, Astrophys J Lett, 700, L43

Geers, V. C., Augereau, J. C., Pontoppidan, K. M. et al. 2006, A&A, 459, 545

Ghosh, P., & Lamb, F. K. 1979, ApJ, 232, 259

Giardino, G., Favata, F., Micela, G. et al. 2007, A&A, 463, 275

Golimowski, D., Ardila, D. R., Krist, J. E. et al. 2006, AJ, 131, 3115

Gómez de Castro, A. I. 1998, Ultraviolet Astrophysics Beyond the IUE final Archive, ESA-SP 413 (Noordwijk, The Netherlands), 59

Gómez de Castro, A. I. 2009, Astrophys Space Sci, 320, 97

Gómez de Castro, A. I., & Pudritz, R. E. 1992, ApJ, 395, 501

Gómez de Castro, A. I., & Pudritz, R. E. 1993, ApJ, 409, 748

Gómez de Castro, A. I., & Verdugo, E. 2003, ApJ, 597, 443

Gómez de Castro, A. I., & Ferro-Fontán, C. 2005, MNRAS, 362, 569

Gómez de Castro, A. I., & von Rekowsky, B. 2011, MNRAS, 411, 849

Goodson, A. P., Winglee, R. M., & Boehm, K. H. 1997, ApJ, 489, 199

Grady, C. A., Woodgate, B., Bruhweiler, F. C. et al. 1999, ApJ, 523, L151

Guedel, M. 2008, Astronomische Nacht, 329, 218

Guedel, M., & Telleschi, A. 2007, A&A, 474, L25

Gullbring, E., Calvet, N., Muzerolle, J. et al. 2000, ApJ, 544, 927

Guenther, E. W., Lehman, H., Emerson, J. P. et al. 1999, A&A, 341, 768

Haisch, K. E., Jr., Lada, E. A., & Lada, Ch. J. 2001, Astronom J, 121, 2065

Hartmann, L. 2009, Protostellar Jets in Context, Astrophysics and Space Science Proceedings Series (New York: Heidelberg), 23

Hartmann, L., & Kenyon, S. J. 1996, ARA&A, 34, 207

Hartmann, L., Calvet, N., Allen, L. et al. 1999, Astronom J, 118, 1784

Hasegawa, T. I., & Herbst, E. 1993, MNRAS, 261, 83

Hasegawa, T. I., Herbst, E., & Leung, Ch. M. 1992, Astrophys J Suppl Series, 82, 167

Hawley, J. F., Gammie, Ch. F., & Balbus, S. A. 1995, ApJ, 440, 742

Hawley, J. F. 2009, Astrophysics and Space Science, 320, 107

Heathcote, S., Morse, J. A., Hartigan, P. et al. 1996, ApJ, 112, 1150

Hester, J. J., & Desch, S. J. 2005, Chondrites and the Protoplanetary Disk, eds. A. N. Krot, Edward R. D. Scott, & Bo Reipurth. ASP Conference Series, 341, 117

Herbig, G. H., & Bell, K. R., 1988, Lick Observatory Bulletin, 1111, 90

Herczeg, G. J., Linsky, J. L., Valenti, J. A. et al. 2002, ApJ, 572, 310

Herczeg, G. J., Wood, B. E., Linsky, J. L. et al. 2004, ApJ, 607, 369

Hillenbrand, L. A., & White, R. J. 2004, ApJ, 616, 998

Hollenbach, D., Johnstone, D., Lizano, S. et al. 1994, ApJ, 428, 654

Iben, I., Jr. 1965, ApJ, 141, 993

Igea, J., & Glassgold, A. E. 1999, ApJ, 518, 848

Iglesias, C. A., & Rogers, F. J. 1996, ApJ, 464, 943

Ilgner, M., & Nelson, R. P. 2006, A&A, 445, 205

Ilgner, M., & Nelson, R. P. 2008, A&A, 483, 815

Ingleby, L., Calvet, N., Bergin, E. et al. 2009, Astrophys J Lett, 703, L137

Johns-Krull, C. M., Valenti, J. A., & Koresko, C. 1999, ApJ, 516, 900

Johns-Krull, C. M., Valenti, J. A. et al. 2004, ApJ, 617, 1204

Kalas, P., Graham, J. R., Clampin, M. C. et al. 2006, ApJ, 637, L58

Kalas, P., Fitzgerald, M. P., & Graham, J. R. 2007, ApJ, 661, L86

Kalas, P., Graham, J. R., Chiang, E. et al. 2008, Science, 322, 1345

Kessler-Silacci, J. E., Hillenbrand, L. A., Blake, G. A. et al. 2005, ApJ, 622, 404

Kirk, J. M., Ward-Thompson, D., André, P. 2005, MNRAS, 360, 1506

Koenigl, A. 1991, ApJ, 370, L39

Krist, J. E., Burrows, C. J., Stapelfeldt, K. R. et al. 1997, ApJ, 481, 447

Krist, J. E., Ardila, D. R., Golimowski, D. A. et al. 2005, AJ, 129, 1008

Lamb, J. K., 1989, Timing Neutron Stars (Dordrecht: Kluwer), 649

Lamzin, S., 1998, Astronomy Rep, 42, 322

Laor, A., & Draine, B. T. 1993, ApJ, 402, 441

Larson, R. B. 1969, MNRAS, 145, 271

Laughlin, G., & Bodenheimer, P. 1994, ApJ, 436, 335

Leinert, Ch., van Boekel, R., Waters, L. B. F. M. et al. 2004, A&A, 423, 537

Lignieres, F., Catala, C., & Mangeney, A. 1996, A&A, 314, 465

Lin, D. N. C., & Papaloizou, J. C. B. 1996, ARA&A, 34, 703

Lin, S. Y., Ohashi, N., Lin, J. et al. 2006, ApJ, 645, 1297

Looney, L. W., Tobin, J. J., & Kwon, W. 2007, ApJ, 670, L131

Liseau, R., Ceccarelli, C., Larsson, B. et al. 1996, *Astronomy and Astrophysics*, 315, L181

Lynden-Bell, D., & Pringle, J. E. 1974, MNRAS, 168, 603

Mace, G. N., Prato, L., & Wasserman, L. H. 2009, Astronom J, 137, 3487

Mannings, V., & Sargent, A. I. 2000, ApJ, 529, 391

Martin-Zaidi, C., Deleuil, M., Le Bourlot, J. et al. 2008, A&A, 484, 225

Mathis, J. S., Rumpl, W., & Nordsieck, K. H. 1977, ApJ, 217, 425

Mayor, M., & Mermilliod, J. C. 1991, Angular momentum evolution of young stars, in Proceedings of the NATO Advanced Research Workshop on Angular Momentum Evolution of Young Stars, held in Noto, Sicily, Italy (Boston: Kluwer), 143

McKee, C. F. 1989, ApJ, 345, 782

Meeus, G., Waters, L. B. F. M., Bouwman, J. et al. 2001, A&A, 365, 476

Mejía, A. C., Durisen, R. H., Pickett, M. K. et al. 2005, ApJ, 619, 1098

Mihalas, D., Dappen, W., & Hummer, D. G. 1988, ApJ, 331, 815

Miesch, M. S. 2005, Living Reviews in Solar Physics, 2, 1

Millan-Gabet, R., Schloerb, F. P., & Traub, W. A. 2001, ApJ, 546, 358

Millan-Gabet, R., Malbet, F., Akeson, R. et al. 2007, Protostars and Planets V, Vol. 951 (Tucson: University of Arizona Press), 539

Muzerolle, J., Calvet, N., & Hartmann, L. 1998, ApJ, 492, 743

Myers, P. C., & Goodman, A. A. 1988, ApJ, 326, L27

Myers, P. C., Adams, F. C., Chen, H. et al. 1998, ApJ, 492, 703

Najita, J., Carr, J. S., & Mathieu, R. D. 2003, ApJ, 589, 931

Natta, A., Prusti, T., Neri, R., et al. 2001, A&A, 371, 186

Onishi, T., Mizuno, A., Kawamura, A. et al. 2002, ApJ, 575, 950

Oppenheimer, M., & Dalgarno, A. 1974, ApJ, 192, 29

O'Sullivan, M., Truss, M., Walker, C. et al. 2005, MNRAS, 358, 632

Padgett, D. L., Brandner, W., Stapelfeldt, K. R. et al. 1999, AJ, 117, 1490

Pedersen, A., & Gómez de Castro, A. I. 2011, ApJ, in press

Pelletier, G., & Pudritz, R. E. 1992, ApJ, 394, 117

Perrot, C. A., & Grenier, I. A. 2003, A&A, 404, 519

Petrov, P. P., Gahm, G. F., Gameiro, J. F. et al. 2001, A&A, 369, 993

Poeppel, W. 1997, Fundam Cosmic Phys, 18, 1

Pollack, J. B., Hollenbach, D., Beckwith, S. et al. 1994, ApJ, 421, 615

Pols, O. R., Tout, C. A., & Eggleton, P. P. 1995, MNRAS, 274, 964

Praderie, F., Catala, C., & Simon, T. 1986, ApJ, Part 1, 303, 311

Preibisch, Th., Ossenkopf, V., Yorke, H. W., et al. 1993, A&A, 279, 577

Prosser, C. F. 1992, Astronom J, 103, 488

Pudritz, R. E., Ouyed, R., Fendt, Ch. et al. 2007, in Protostar and Planets V, eds. B. Reipurth, D. Jewitt, & K. Keil (Tucson: University of Arizona Press), 277

Ray, T. P., Muxlow, T. W. B., Axon, D. J. et al. 1997, Nature, 385, 415

Raymond, J. C., Blair, W. P., & Long, K. S. 1997, ApJ, 489, 314

Reipurth, B, Chun Yu, K., Rodrguez, L. F. et al. 1999, Astron Astrophys, 352, L84

Reipurth, B., 1999, General Catalogue of Herbig-Haro Objects, available through the Vizier service at vizier.u-strasbg.fr

Reipurth, B., Bally, J., Fesen, R. A. et al. 1998, Nature, 396(6709), 343

Rettig, T., Brittain, S., Simon, T. et al. 2006, ApJ, 646, 342

Rice, W. K. M., Lodato, G., & Armitage, P. J. 2005, MNRAS, 364, L56

Roberge, A., Feldman, P. D., Weinberg, A. J. et al. 2006, Nature, 441, 724

Rogers, F. J., Swenson, F. J., & Iglesias, C. A. 1996, ApJ, 456, 902

Romanova, M. M., Ustyugova, G. V., Koldoba, A. V. et al. 2004, ApJ, 610, 920

Rotstein, N., & Gimenez de Castro, C. G. 1996, ApJ, 464, 859

Safier, P. N. 1993, ApJ, 408, 148

Sargent, B., Forrest, W. J., Tayrien, C. et al. 2009, ApJ, 690, 1193

Saumon, D., Chabrier, G., & van Horn, H. M. 1995, Astrophys J Suppl Series, 99, 713

Semenov, D., Wiebe, D., & Henning, Th. 2004, A&A, 417, 93

Shakura, N. I., & Sunyaev, R. A. 1973, A&A, 24, 337

Shirley, Y. L., Evans, N. J., II., Rawlings, J. M. C. et al. 2000, Astrophys J Suppl Series, 131, 249

Shirley, Y. L., Evans, N. J., II., Young, K. E. et al. 2003, Astrophys J Suppl Series, 149, 375

Shu, F., Najita, J., Shang, H. et al. 2000, in Protostars and Planets IV, eds. V. Mannings, A. P. Boss, & S. S. Russell (Tucson: University of Arizona Press), 789

Shuping, R. Y., Bally, J., & Morris, M. 2003, ApJ, 587, L109

Siess, L., Forestine, M., & Dougados, C., 1997, A&A, 324, 556

Siess, L., Dufour, E., & Forestini, M. 2000, A&A, 358, 593

Simon, M., Dutrey, A., & Guilloteau, S. 2000, ApJ, 545, 1034

Snell, R. L., Loren, R. B., & Plambeck, R. L. 1980, ApJ, 329, L17

Stassun, K. G., Mathieu, R. D., & Vaz, L. P. R. 2004, Astrophys J Suppl Series, 151, 357

Stauffer, J. R., Balachandran, S. C., Krishnamurthi, A. et al. 1997, ApJ, 475, 604

Stempels, H. C., & Piskunov, N. 2002, A&A, 391, 595

Tappe, A., Lada, C. J., Black, J. H. et al. 2008, ApJ, 680, L118

Toomre, A. 1964, ApJ, 139, 1217

Turner, N. J., & Drake, J. F. 2009, ApJ, 703, 2152

Turner, N. J. J., Bodenheimer, P., & Bell, K. R. 1997, ApJ, 480, 754

van Boekel, R., Waters, L. B. F. M., Dominik, C. et al. 2004, A&A, 418, 177

Van Zadelhoff, G.-J., Aikawa, Y., & Hogerheijde, M. R. 2003, A&A, 397, 789

Vasyunin, A. I., Semenov, D., Henning, Th. et al. 2008, ApJ, 672, 629

Von Rekowski, B., & Brandenburg, A. 2006, Astronomische Nachrichten, 327, 53

Watson, A. M., Stapelfeldt, K. R., & Wood, K. 2007, Protostars and Planets V, Vol. 951 (Tucson: University of Arizona Press), 523

Weber, E. J., & Davis, L., Jr. 1967, ApJ, 148, 217

Wilkinson, E., Harper, G. M., Brown, A. et al. 2002, Astronom J, 124, 1077

Woodall, J., Agúndez, M., Markwick-Kemper, A. J. et al. 2007, A&A, 466, 1197

Wu, Y., Wei, Y., Zhao, M. et al. 2004, A&A, 426, 503

Yorke, H. W., & Bodenheimer, P. 1999, ApJ, 525, 330

Yorke, H. W., & Sonnhalter, C. 2002, ApJ, 569, 846

Young, Ch. H., & Evans, N. J., II. 2005, ApJ, 627, 293

Zhang, Q., Hunter, T. R., Barnd, J. et al. 2005, ApJ, 635, 864